


Arc Blanc: a real time ocean simulation framework

David Algis 
Université de Poitiers
and Studio Nyx

Bérenger Bramas
INRIA Nancy

Emmanuelle Darles
Université de Poitiers

Lilian Aveneau
Université de Poitiers



Figure 1. Example of rendering of the Arc Blanc framework.

Abstract

The oceans cover the vast majority of the Earth. Therefore, their simulation has many scientific, industrial and military interests, including computer graphics domain. By fully exploiting the multi-threading power of GPU and CPU, current state-of-the-art tools can achieve real-time ocean simulation, even if it is sometimes needed to reduce the physical realism for large scenes. Although most of the building blocks for implementing an ocean simulator are described in the literature, a clear explanation of how they interconnect is lacking. Hence, this paper proposes to bring all these components together, detailing all their interactions, in a comprehensive and fully described real-time framework that simulates the free ocean surface and the coupling between solids and fluid. This article also presents several improvements to enhance the physical realism of our model. The two main ones are: calculating the real-time velocity of ocean fluids at any depth; computing the input of the fluid to solid coupling algorithm.

1. Introduction

1.1. Context

Simulating the dynamics of an ocean and its surrounding elements remains an important objective in computer graphics. As all the oceans encompass a substantial portion of the Earth's surface, understanding their behavior is of paramount importance in scientific, industrial, entertainment and military fields.

The computational power of modern GPUs and CPUs, coupled with the latest high-speed memory, has greatly simplified the processing of fluid dynamics simulations. They make it possible to perform real-time simulations on large discrete grids surrounded by solids, albeit with some physical approximations, thanks to their massively parallel capabilities.

While there are many articles describing different parts of ocean simulation, the literature lacks papers that bring all the pieces together. This article proposes a fully described real-time framework designed to simulate the free surface of the ocean and the interactions between solid objects and the surrounding fluid in real time (see Figure 2). This new framework incorporates three different methods from the literature:

- The simulation of the free surface of the ocean, initially developed by Tessendorf (2001) [Tessendorf d] and its improvements along the years [Horvath; Tessendorf b].
- The estimation of the forces applied by the fluid on a solid mesh, mixing together different techniques [Yuksel; Kellomäki].
- The simulation of the alteration of a free surface by a solid, inspired by Cords and Staadt works (2009) [Cords and Staadt].

To bring together these previous works, this new framework proposes two new contributions:

- An algorithm to compute the ocean velocity at any depth from the simulation of the free surface. This velocity is applied to the fluid to solid forces.
- An algorithm to compute the input of the Cords and Staadt method more realistically from the free surface.

This article is organized as follows. Section 2 presents the previous works related to ocean simulation, including its interaction with solid. Sections 3 to 5 detail the Arc Blanc framework, including the ocean surface simulation in Section 3, the action of the fluid to solids in Section 4 and the action of a solid to the fluid in Section 5. Section 6 discusses some results obtained with the Arc Blanc framework. At last, Section 7 gives general conclusions.

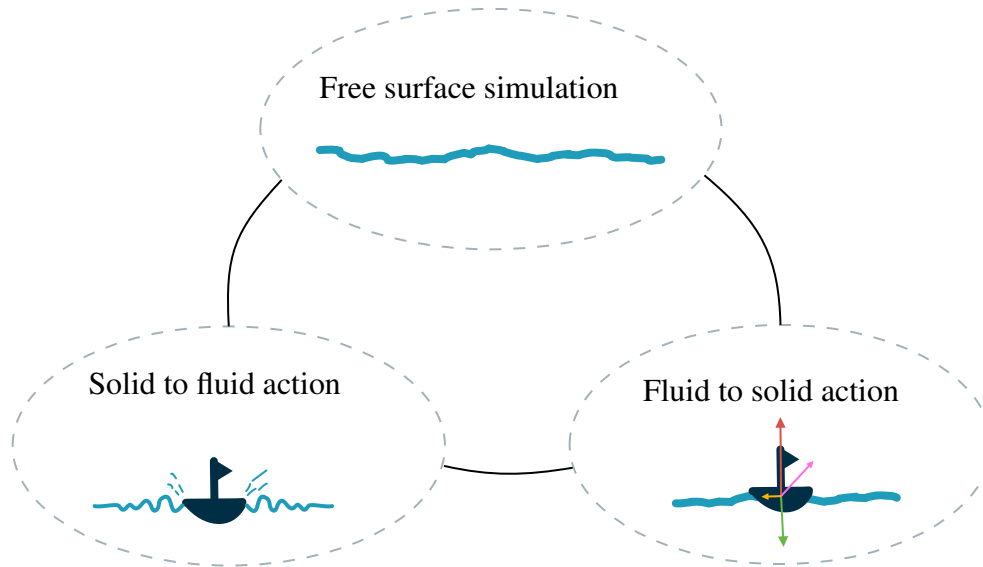


Figure 2. Overview of the Arc Blanc framework components: free surface, solid to fluid and fluid to solid coupling.

2. Related works

This section presents the main works related to the simulation of ocean, including the free surface, the fluid to solid and solid to fluid coupling.

2.1. Ocean free surface simulation

J. Tessendorf (2001) [Tessendorf d] presented what could be considered a seminal work in real-time ocean simulation. His work relies on the Fast Fourier Transform (FFT) and statistical wave spectra to accurately find the analytical solution to an approximation of the Navier-Stokes equations on a 2D height field. This method is commonly known as the “Tessendorf method”.

The realism of this method was significantly improved by Horvath (2015) [Horvath], who proposed an empirically based directional spectrum. In addition, he proposed to add a parameter called “swell”, which allows the transition from empirical directional propagation to parallel waves.

Another notable improvement of Tessendorf’s method is the reduction of artifact effects through the use of multiple displacement layers. This technique, introduced by Dupuy and Bruneton (2012) [Dupuy and Bruneton], involves stacking multiple displacement layers, each one representing different scales of wave motion. By combining these layers, the artifacts and repetitive patterns that can often occur in simulated water surfaces are effectively reduced or eliminated. Finally, Tessendorf (2017) [Tessendorf b] summarized these works in a prototype framework for large-scale water simulation.

The Arc Blanc framework aggregates all these methods in order to simulate the ocean free surface.

2.2. Fluid to solid coupling

There are several ways to describe the motion of a solid in a given fluid. Many particle-based methods have been developed in recent years, as presented by Koschier *et al.* (2022) [Koschier et al.]. Akinci *et al.* (2012) [Akinci et al.] have proposed to calculate contact forces between fluid particles and boundary ones in combination with Predictive-Corrective Incompressible Smoothed Particles Hydrodynamics (PCISPH) [Solenthaler and Pajarola]. Ihmsen *et al.* (2014) [Ihmsen et al.] have applied the same principle to Implicit Incompressible SPH (IISPH), and Bender and Koschier (2017) [Bender and Koschier] to Divergence Free SPH (DFSPH). These works have been improved and stabilized by Gissler *et al.* [Gissler et al.]. These methods look promising because of their physical accuracy. Nevertheless, their performance is linked to the number of particles used for the simulation, which makes them impossible to apply in real time for large scale environments.

Another approach related to the dynamics of a ship in water is the calculation of the so-called *Response Amplitude Operator* (RAO), which is expressed using strip theory by Salvesen *et al.* (1970) [Salvesen et al.]. Fonseca and Guedes Soares (1998) [Fonseca and Soares] improved the method to support more nonlinear effects and large amplitude motions. Varela and Guedes Soares (2011) [Varela and Guedes Soares] have used a table of pre-calculated RAO, which are later interpolated to achieve an interactive frame rate. However, to our knowledge, this type of method is either too expensive for real-time simulation or not general enough because it requires some physical pre-computation based on computational fluid dynamics or experimental data.

Finally, another attempt to achieve real-time performance is to approximate the forces induced by the fluid on the solid on a mesh. Basically this is a less accurate method, but it's more efficient and general as it avoids significant pre-calculation. Yuksel (2010) [Yuksel] in his thesis proposed a set of three forces: buoyancy, drag and lift. Kellomäki (2014) [Kellomäki] focused only on buoyancy and drag forces. Casas-Yrurzum *et al.* [Casas-Yrurzum et al.] simulates the motion of speedboats by decomposing the solid as a set of small cubes. Kerner (2016) [Kerner] wrote a full article on boat physics for video games, adding more forces to simulate slamming and linear damping. The Arc Blanc framework relies on these forces approximation, aggregating these four last papers.

2.3. Solid to fluid coupling

The simulation of the surface of water in contact with a solid body has been an active research topic for the last twenty years. Gomez (2000) [Gomez] solved the wave

equation using the finite-difference method (FDM) to simulate waves on the free surface. This method was improved by Cords and Staadt (2009) [Cords and Staadt] to work with moving objects. Tessendorf (2004) [Tessendorf c] proposed a convolutional method. He extended his method by using an exponential solver [Tessendorf a]. Yuksel (2007) [Yuksel et al.] used a Lagrangian paradigm to model the waves as particles, which he called wave-particles. Chentanez and Müller (2010) [Chentanez and Müller] created a hybrid solver combining Eulerian and Lagrangian approaches. Canabal *et al.* (2016) [Canabal et al.] improved the physical accuracy of the convolutional method by introducing a dispersion kernel. Jeschke and Woktan (2017) [Jeschke and Wojtan] took the work of C. Yuksel a bit further by introducing the notion of a wave packet, which carries information about an entire wave train. One year later, Jeschke *et al.* (2018) [Jeschke et al.] proposed to use a wavelet transformation that discretizes the wave amplitudes as a function of space, frequency and direction. Finally, Schreck *et al.* (2019) [Schreck et al.] based their work on the method of fundamental solutions to generate ambient waves on a large scale domain interacting with complex boundaries.

For solid-fluid coupling, the Arc Blanc framework based its calculations on the FDM described in Gomez (2000) [Gomez] and its improvement by Cords and Staadt (2009) [Cords and Staadt], because its ability to be real-time while providing quite realistic behavior.

3. Ocean waves

This section summarizes Tessendorf's method and the various improvements it has received. It also presents our first contribution: calculation of the fluid velocity at any depth.

Let us introduce some notations as follows:

- The scalar $H \in \mathbb{R}^+$ denotes the depth of the water. The Arc Blanc framework assumes **deep water** and therefore supposes that H tends towards $+\infty$ ¹.
- The scalar $h(\mathbf{x}, t) \in \mathbb{R}$ is the height of the water surface at the horizontal position $\mathbf{x} = [x \ z]^T$ and at time t .
- The vector $\mathbf{v}(\mathbf{x}, y, t) = [v_x(\mathbf{x}, y, t) \ v_y(\mathbf{x}, y, t) \ v_z(\mathbf{x}, y, t)]^T \in \mathbb{R}^3$ represents the velocity of the fluid at the horizontal position \mathbf{x} , depth y and time t .
- The scalar $\phi(\mathbf{x}, y, t) \in \mathbb{R}$ is the potential velocity of fluid at the horizontal position \mathbf{x} , depth y and time t .
- The scalar $g = 9.80665 \text{ m.s}^{-2}$ denotes the gravitational acceleration, while $\mathbf{g} \in \mathbb{R}^3$ is the gravitational field.

¹See Appendix A for more details on this assumption.

Tessendorf method is based on the following approximations of the Navier-Stokes equations²:

$$\begin{cases} \frac{\partial \phi}{\partial t} = -gh(\mathbf{x}, t) & \text{for } y = 0, \\ \Delta \phi = 0 & \text{for } -H \leq y \leq 0, \\ \frac{\partial h}{\partial t} = \frac{\partial \phi}{\partial y} & \text{for } y = 0, \\ \frac{\partial \phi}{\partial y} = 0 & \text{for } y = -H. \end{cases} \quad (1)$$

3.1. Water height

Tessendorf (2001) [Tessendorf d] proposed to solve Equation 1 using a sum of waves of different amplitudes and wavelengths as follows:

$$h(\mathbf{x}, t) = \sum_{\mathbf{k}} \tilde{h}(\mathbf{k}, t) \exp(i\mathbf{k} \cdot \mathbf{x}), \quad (2)$$

where $\mathbf{k} = [k_x \ k_z]^T$ is the wave vector with $k_x = \frac{2\pi n}{L_i}$ and $k_z = \frac{2\pi m}{L_i}$, L_i is the length of the i -th cascade as defined in Section 3.3, n and m are integers in $[-\frac{N}{2}, \frac{N}{2}]$, $N \in \mathbb{N}^+$ being a constant given by user, and \tilde{h} is given by:

$$\tilde{h}(\mathbf{k}, t) = \tilde{h}_0(\mathbf{k}) \exp(i\omega(k)t) + \tilde{h}_0^*(-\mathbf{k}) \exp(-i\omega(k)t), \quad (3)$$

where k is the Euclidean norm of the wave vector \mathbf{k} , $\omega(k) = \sqrt{gk}$ is the **dispersion relation**³ and \tilde{h}_0^* the conjugate of \tilde{h}_0 . Researchers in oceanography have made statistical measurements on the ocean to compute \tilde{h}_0 , leading to many different *ocean spectra* [Tessendorf b]. In its original paper, Tessendorf (2001) [Tessendorf d] used the *Phillips Spectrum* with Gaussian fluctuation, leading to the following expression of $\tilde{h}_0(\mathbf{k})$:

$$\tilde{h}_0(\mathbf{k}) = \xi_{\mathbf{k}} \sqrt{\frac{4\pi}{L_i k} S(\omega) D(\omega, \theta) \left| \frac{\partial \omega(k)}{\partial k} \right|} \quad (4)$$

where $\xi_{\mathbf{k}}$ are samples from a Gaussian distribution with mean 0 and standard deviation 1, $S(\omega)$ and $D(\omega, \theta)$ are the frequency and directional spectra described respectively in paragraphs 3.1.1 and 3.1.2.

3.1.1. JONSWAP frequency spectrum

The Arc Blanc framework uses the frequency spectrum developed by Hasselmann *et al.* (1973) [K. Hasselmann] in the Joint North Sea Wave Project (JONSWAP). This spectrum was developed for deep sea water, and hence is in line with our deep water hypothesis. It is expressed as follows:

$$S(\omega) = \frac{\alpha g^2}{\omega^5} \exp\left(-\frac{5}{4} \left(\frac{\omega_p}{\omega}\right)^4\right) \gamma^r \quad (5)$$

where:

²See Appendix B.

³The dispersion relation is defined for deep water, see Appendix A for more details.

- The constant $\alpha = 0.076 \left(\frac{U^2}{Fg} \right)^{0.22}$, U being the wind speed in $m.s^{-1}$ and F the fetch⁴ in m .
- The constant $\omega_p = 22 \left(\frac{g^2}{UF} \right)$.
- The constant $\gamma = 3.3$.
- The exponent term r is defined as follows:

$$r = \exp \left(-\frac{(\omega - \omega_p)^2}{2\sigma^2\omega_p^2} \right) \quad (6)$$

- The term σ is as follows:

$$\sigma = \begin{cases} 0.07 & \omega \leq \omega_p, \\ 0.09 & \omega > \omega_p. \end{cases}$$

3.1.2. Custom Donelan-Banner spectrum

In the Arc Blanc framework, the directional spectrum relies on the work of Horvath (2015) [Horvath], that mixes together the Donelan-Banner spectrum to control the direction of the waves and a “swell parameter”. Let us recall that, if the wind direction is given by θ_0 , the wind direction bias θ can be defined as follows:

$$\theta = \text{atan2}(k_z, k_x) - \theta_0 \quad (7)$$

Moreover, the Donelan-Banner D_{DB} spectrum is given as follows:

$$D_{DB}(\omega, \theta) = \frac{1}{2} Q_{DB}(\omega) \beta_s (\text{sech}(\beta_s \theta))^2. \quad (8)$$

This expression depends on the ratio $r_\omega = \omega/\omega_p$ of ω and ω_p , the latter being the same as in JONSWAP spectrum. Hence, in the Arc Blanc framework β_s is defined as a mix of Donelan *et al.* (1985) [Donelan et al.] for $r_\omega < 1.6$, and Banner (1990) [Banner] for $r_\omega \geq 1.6$. Moreover, the case $r_\omega < 0.56$ is removed, as suggested by C. Horvath. Altogether, this leads to the following expression of β_s :

$$\beta_s = \begin{cases} 2.61 (r_\omega)^{1.3} & \text{for } r_\omega < 0.95 \\ 2.28 (r_\omega)^{-1.3} & \text{for } 0.95 \leq r_\omega < 1.6 \\ 10^\epsilon & \text{for } r_\omega \geq 1.6 \end{cases} \quad (9)$$

where

$$\epsilon = 0.8393 \exp(-0.567 \ln(r_\omega^2)) - 0.4. \quad (10)$$

⁴The fetch is the length of the area over which the wind is acting on the water, that is to say the distance from a lee shore.

Any directional spectrum $D(\omega, \theta)$ must satisfy the normalization condition:

$$\int_{-\pi}^{\pi} D(\omega, \theta) d\theta = 1 \quad (11)$$

Hence, $Q_{DB}(\omega)$ is a normalization factor to make $D_{DB}(\omega, \theta)$ respect condition 11:

$$Q_{DB}(\omega) = \frac{1}{\int_{-\pi}^{\pi} \frac{1}{2} \beta_s (\text{sech}(\beta_s \theta))^2 d\theta} = \frac{1}{\tanh(\beta_s \pi)} \quad (12)$$

The Arc Blanc framework simulates swell, corresponding to more elongated waves that have traveled out of their generating area and that mixes with wind-generated local waves. As in Horvath (2015) [Horvath], it relies on the swell parameter ξ related to the spectrum D_ξ , defined as follows:

$$D_\xi(\omega, \theta) = |\cos(\theta/2)|^{2s_\xi} \quad (13)$$

where the spreading swell function s_ξ is defined by:

$$s_\xi = 16 \tanh(1/r_\omega) \xi^2 \quad (14)$$

Note that, with $\xi = 0$, the spectrum $D_0(\omega, \theta) = \frac{1}{2\pi}$ is constant while for $\xi = 1$ the waves become much more elongated.

The product between the Donelan-Banner and D_ξ spectra is denoted by $D_{DB\xi}$, and is expressed as follows:

$$D_{DB\xi}(\omega, \theta) = Q_{DB\xi}(\omega) D_{DB}(\omega, \theta) D_\xi(\omega, \theta) \quad (15)$$

where the normalization factor is:

$$Q_{DB\xi}(\omega) = \frac{1}{\int_{-\pi}^{\pi} D_{DB}(\omega, \theta) D_\xi(\omega, \theta) d\theta}. \quad (16)$$

This normalization factor $Q_{DB\xi}(\omega)$ is computationally expensive.

It can be noticed that it depends only on the ratio r_ω . Hence, the Arc Blanc framework uses a simple method to approximate it, through interpolations relying on multiple Lagrangian polynomials as follows:

$$\widetilde{Q_{DB\xi}}(r_\omega) = \begin{cases} 7.1467551r_\omega^2 - 13.4662001r_\omega + 7.75651088 & \text{for } r_\omega < 0.94, \\ -0.69906109r_\omega^2 + 0.77975933r_\omega + 0.10169164 & \text{for } 0.94 \leq r_\omega < 5, \\ -2.1860997r_\omega^2 + 0.0269209r_\omega + 0.00016283 & \text{for } 5 \leq r_\omega < 100, \\ 1.2038847r_\omega + 0.0008147 & \text{else.} \end{cases} \quad (17)$$

Computed using 10000 random samples, the normalization integral (Equation 11) of such an approximation is 1.0699 in average.

Note that a first normalization factor Q_{DB} is applied to the Donelan-Banner spectrum (Equation 8) before calculating the second normalization factor $\widetilde{Q_{DB\xi}}(r_\omega)$. In fact, a normalization problem will occur if the full-spectrum normalization factor is simply approximated before its application, because for small values of r_ω , $Q_{DB\xi}(\omega)$ will be very low and therefore numerically challenging to normalize.

Finally, the Arc Blanc framework uses a last parameter $\delta \in [0, 1]$ that represents how much the waves orientation is constant ($\delta = 0$) or not ($\delta = 1$) (see Figure 3). Its meaning is as follows:

- $\delta = 0$ indicates a *neutral* directional spectrum, that has no consequence on \tilde{h}_0 ;
- $\delta = 1$ indicates a spectrum equals to $D_{DB\xi}(\omega, \theta)$.

This gives the final expression of the custom Donelan-Banner spectrum used in the Arc Blanc framework:

$$D(\omega, \theta) = (1 - \delta) \frac{1}{2\pi} + \delta D_{DB\xi}(\omega, \theta). \quad (18)$$

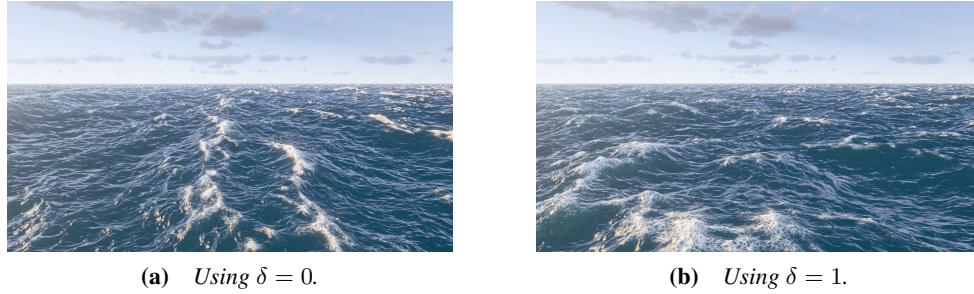


Figure 3. Effect of the parameter δ on sea state 5 on the Beaufort scale.

3.2. Water displacement and derivative

The Arc Blanc framework uses the horizontal displacement $\mathbf{D}(\mathbf{x}, t) = [D_x(\mathbf{x}, t) \ D_z(\mathbf{x}, t)]^T$ of seawater to simulate more realistic choppy waves. As proposed in Sections 4.5 and 4.6 of Tessendorf (2001) [Tessendorf d], it is calculated as follows:

$$\mathbf{D}(\mathbf{x}, t) = \sum_{\mathbf{k}} \tilde{\mathbf{D}}(\mathbf{k}, t) \exp(i\mathbf{k} \cdot \mathbf{x}) \quad (19)$$

where

$$\tilde{\mathbf{D}}(\mathbf{k}, t) = \left[\tilde{D}_x(\mathbf{k}, t) \ \tilde{D}_z(\mathbf{k}, t) \right]^T = \frac{i\mathbf{k}}{k} \tilde{h}(\mathbf{k}, t). \quad (20)$$

Furthermore, to obtain additional details on the sea surface (*e.g.* foam positions, normal vectors...) the derivative of the horizontal and vertical displacements must be computed, respectively of $\mathbf{D}(\mathbf{x}, t)$ and $h(\mathbf{x}, t)$. Taking advantage of the symmetry $\frac{\partial D_z}{\partial x}(\mathbf{x}, t) = \frac{\partial D_x}{\partial z}(\mathbf{x}, t)$, this relies on five derivatives only:

$$\begin{aligned}\frac{\partial D_x}{\partial x}(\mathbf{x}, t) &= \sum_{\mathbf{k}} -ik_x \tilde{D}_x(\mathbf{k}, t) \exp(i\mathbf{k} \cdot \mathbf{x}), \\ \frac{\partial D_z}{\partial x}(\mathbf{x}, t) &= \sum_{\mathbf{k}} -ik_x \tilde{D}_z(\mathbf{k}, t) \exp(i\mathbf{k} \cdot \mathbf{x}), \\ \frac{\partial D_z}{\partial z}(\mathbf{x}, t) &= \sum_{\mathbf{k}} -ik_z \tilde{D}_z(\mathbf{k}, t) \exp(i\mathbf{k} \cdot \mathbf{x}), \\ \frac{\partial h}{\partial x}(\mathbf{x}, t) &= \sum_{\mathbf{k}} k \tilde{D}_x(\mathbf{k}, t) \exp(i\mathbf{k} \cdot \mathbf{x}), \\ \frac{\partial h}{\partial z}(\mathbf{x}, t) &= \sum_{\mathbf{k}} k \tilde{D}_z(\mathbf{k}, t) \exp(i\mathbf{k} \cdot \mathbf{x}).\end{aligned}$$

3.3. Cascades

While the expression of the water height in Equation 2 is convenient, it may result in an ocean surface that appears overly repetitive. A naive solution to handle this problem consists in using a huge resolution N , but it has a major impact on performance. The Arc Blanc framework uses the more efficient solution proposed by Dupuy and Bruneton (2012) [Dupuy and Bruneton]. It consists in dividing the spectrum into c layers or *cascades* of different lengths. Each of these layers represents a different wavelength in Equation 2. The length of the i -th cascade is denoted by L_i . These lengths L_i are parameters in the expression of the wave vector component described in Equation 2. Moreover, the different cascades are cut off at arbitrary value to avoid overlap between them, as illustrated in Figure 4.

The Arc Blanc framework uses by default 3 cascades with the following settings:

- $L_0 = 256$ operating for waves length $k \in [0, \frac{12\pi}{16}]$
- $L_1 = 16$ operating for waves length $k \in [\frac{12\pi}{16}, \frac{12\pi}{4}]$
- $L_2 = 4$ operating for waves length $k \in [\frac{12\pi}{4}, +\infty]$.

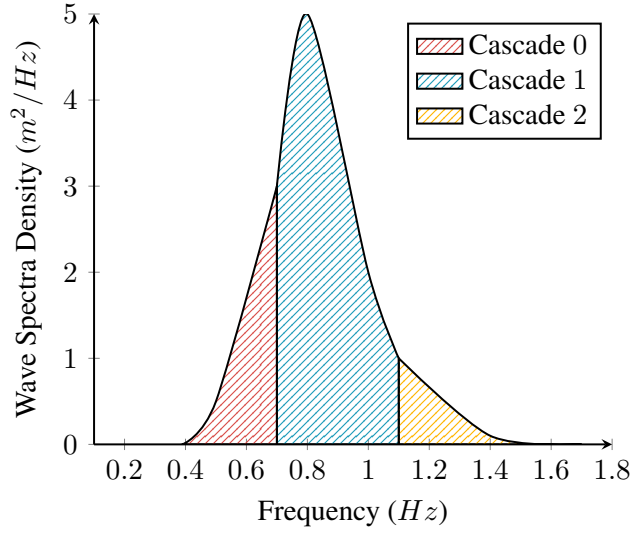


Figure 4. Example of a spectrum split into 3 different cascades: each cascade operates on a different interval of wave vector length.

3.4. Velocity of water

Starting from the system 1, the Arc Blanc framework proposes to compute the velocity of the water at any depth y , as follows⁵:

$$\mathbf{v}(\mathbf{x}, y, t) = \sum_{\mathbf{k}} \tilde{\mathbf{v}}(\mathbf{k}, y, t) \exp(i\mathbf{k} \cdot \mathbf{x}), \quad (21)$$

where the vector $\tilde{\mathbf{v}}(\mathbf{k}, y, t)$ is given as follows:

$$\tilde{\mathbf{v}}(\mathbf{k}, y, t) = E(\mathbf{k}, y) \left(\tilde{h}_0(\mathbf{k}) \exp(i\omega(k)t) - \tilde{h}_0^*(-\mathbf{k}) \exp(-i\omega(k)t) \right) \begin{bmatrix} \frac{-k_x g}{\omega(k)} \\ i\omega(k) \\ \frac{-k_z g}{\omega(k)} \end{bmatrix}, \quad (22)$$

where the attenuation function $E(\mathbf{k}, y) \in \mathbb{R}$ is defined as follows:

$$E(\mathbf{k}, y) = \begin{cases} 1 + ky & \text{if } y > 0, \\ \exp(ky) & \text{else.} \end{cases} \quad (23)$$

The first case ($y > 0$) comes from an extrapolation above the sea surface of the normal case ($y \leq 0$).

To our knowledge, this expression of the velocity has never been used in a real time ocean simulator before.

⁵See Appendix A for more details on the origin of this expression

3.5. Waves' height implementation details

This section gives some technical details of the implementation of an ocean with Tessendorf's method in the Arc Blanc framework.

First, it should be noticed that the expressions of the ocean surface's height (Equation 2), the displacements (Equation 19) and their five derivatives, and the velocity (Equation 21) have "a form of an inverse discrete Fourier transform". More precisely, the **frequency space** coefficients appearing before the term $\exp(i\mathbf{k} \cdot \mathbf{x})$ are stored in a square matrix of size $N \times N$, for each expression. Then, the full sum is computed through an **inverse fast Fourier transform** (IFFT) applied on this coefficients' matrix. In the Arc Blanc framework, this trick allows computing these eight expressions without any significant impact on performance, even for huge domains.

Second, as the Arc Blanc framework simulates a tile of water of size $N \times N$ using c cascades, it stores the height, the displacement, and other relevant data in a 1D array of size c , where each entry contains a 2D array of size $N \times N$. The Arc Blanc framework computes efficiently these values on the GPU, with dedicated kernel that are launched with a grid of threads structured as $N \times N \times c$. Specifically, $N \times N$ threads are assigned to the x and y dimensions to cover the spatial resolution of the water tile, while c threads along the z dimension correspond to the different cascades. This approach ensures that computations for all cascades are executed in parallel.

Third, many terms are independent on the time t : $\tilde{h}_0(\mathbf{k})$, $\tilde{h}_0^*(-\mathbf{k})$ and the wave data (\mathbf{k} and $\omega(k)$). The Arc Blanc framework computes them for each cascade wave vector at each spectrum change only, but not at each iteration. Then it does a combination with time-dependent terms at each iteration, giving an expression for the coefficients in frequency space for the eight IFFT.

To compute the water height at a specific point, it is not sufficient to directly evaluate Equation 2 after performing the IFFT. This is because the water surface is described parametrically, with fluid positions depending on both horizontal and vertical displacements, as detailed in Section 3.2. Accurately determining the water surface position at a given horizontal location requires an iterative process (see Algorithm 1): the estimated position is adjusted by subtracting the displacement vector, and the water height is recalculated until convergence. However, in practice, waiting for full convergence may be computationally expensive. Instead, the loop is limited to $N_{iter} = 4$ iterations, a value chosen to balance accuracy and performance (see Appendix D for details on this choice).

Last but not least, one might think that applying IFFT should be enough to get the expected result. Nevertheless, using the standard IFFT algorithm (such as the one of Cooley and Tukey (1965) [Cooley and Tukey]) leads to some incorrect geometry changes. Unlike usual IFFT, the used range is $[-N/2, N/2]$ and so the wave vectors have negative components (*e.g.* the height). To fit with the theory of Fourier transforms, in the Arc Blanc framework each value at index i, j of the 2D matrices is

Algorithm 1 Iterative Retrieval of Water Height

Require: A position \mathbf{x} to evaluate the water height and the horizontal and vertical displacements: $\mathbf{D}(\mathbf{x}, t)$, $h(\mathbf{x}, t)$

- 1: Initialize displacement $\mathbf{W} = (0, 0, 0)$
- 2: **for** $k = 1$ to N_{iter} **do** // Iterative correction to account for displacement
- 3: Compute shifted position: $\mathbf{W} = \mathbf{x} - \mathbf{W}$
- 4: Compute horizontal displacement at \mathbf{W} // The sum of bilinear interpolation of the displacement on each cascades
- 5: **end for**
- 6: **return** The vertical component of \mathbf{W}

multiplied by $(-1)^{i+j}$.

In the Arc Blanc framework, the number of IFFT applications is divided by two using Theorem 1 on Hermitian matrices⁶ (see annex C for its proof).

Theorem 1. *Let: $X = (x_{n,m}), Y = (y_{n,m}) \in M_n(\mathbb{C})$ be two Hermitian matrices. Then the following relation is valid:*

$$\mathcal{F}^{-1}(X + iY) = \Re(\mathcal{F}^{-1}(X)) + i\Re(\mathcal{F}^{-1}(Y)) \quad (24)$$

Hence, in the Arc Blanc framework the coefficients in frequency space of two Hermitian matrices X and Y are combined in a single matrix $H = X + iY$. Using Theorem 1, one complex IFFT suffices to obtain the real parts of two IFFT $\mathcal{F}^{-1}(X)$ and $\mathcal{F}^{-1}(Y)$. This treatment allows reducing IFFT computation times by a factor close to 2.

3.6. Waves' velocity implementation details

Contrary to the displacement and its derivative which are height maps and 2D functions, the velocity must be known in 3D space. Hence, its calculation is more difficult and requires more computation time. Computing the velocity for all the points of a 3D grid, or even only the points where it must be evaluated for fluid to solid coupling (Section 2.2) is not possible in real-time, as it involves a large to huge number of IFFT. Unfortunately, the dependency of the attenuation (Equation 23) on both the wave vectors and y makes the depth dependency of the velocity fundamentally tied to the wave vector, preventing any simplifications that could reduce the required calculations.

To reduce the complexity of this problem, the Arc Blanc framework opts for an interpolation scheme, involving a reasonable number of IFFTs that is proportional to the size of the discretization.

⁶A matrix $X = (x_{n,m})$ is Hermitian if it is equal to its own conjugate transpose: $X = X^\dagger$ or $x_{n,m} = x_{m,n}^*$.

More concretely, the velocity must be computed at any horizontal position in $I = [y_{min}, y_{max}]$. In the Arc Blanc framework, d growing depths y_i are chosen in this interval I . For each of these depths y_i , the i -th velocity $\mathbf{v}_i(\mathbf{x}, y_i, t)$ is computed using one IFFT, leading to d IFFTs for all the sampled depths y_i . Then, the velocity $\mathbf{v}(\mathbf{x}, y, t)$ at any depth $y \in I$ is computed using an ad hoc interpolation from the different \mathbf{v}_i .

A first way to do this interpolation mechanism relies on a linear scheme. Nevertheless, it produces a very inaccurate result. Hence, the Arc Blanc framework uses an exponential scheme made on logarithmic sampling of the interval I . They are discussed in the next two sections.

3.6.1. Exponential interpolation

The vertical dependency of velocity links to the exponential attenuation function from Equation 23. Hence, instead of a linear interpolation the Arc Blanc framework uses an exponential interpolation $f_e(x)$ that should resemble the following expression:

$$f_e(x) = \alpha \exp(\beta x). \quad (25)$$

Knowing $f_e(a) = f(a)$ and $f_e(b) = f(b)$, it is straightforward to obtain the two values α and β as follows:

$$\begin{cases} \alpha = \frac{f(a)}{\exp(\beta a)} \\ \beta = \frac{\ln(|f(b)|) - \ln(|f(a)|)}{b - a} \end{cases} \quad (26)$$

This exponential interpolation function $f_e(x)$ is applied to extract the magnitude and rotation angle of the velocity $\mathbf{v}(\mathbf{x}, y, t)$.

3.6.2. Logarithmic distribution

As the velocity decays exponentially with depth, the ones close to the ocean surface play a more important role in accuracy than the one at the bottom of the ocean. Hence, a regular sampling along the depth seems inappropriate, albeit the exponential interpolation.

The Arc Blanc framework uses the following logarithmic distribution:

$$l_d(y_i) = \begin{cases} \beta \ln(\alpha |y_i|^2 + 1) & \text{if } y_i > 0 \\ -\beta \ln(\alpha |y_i|^2 + 1) & \text{if } y_i \leq 0 \end{cases} \quad (27)$$

where $\alpha = 0.0001$ and $\beta = -y_{min} / (2 \ln(\alpha |y_{min}|^2 + 1))$.

This distribution is designed based on the following considerations. First, while the velocity decays exponentially, it relies on a logarithmic function similar to $y_i \mapsto \ln(|y_i| + 1)$. Since this function transforms the negative y_i into a positive one, the

result is multiplied by the sign of y_i . Also, this function decreases slowly (actually with $\ln(250) = 5.5$), hence the logarithmic distribution uses the square of $|y_1|$. Lastly, the parameter α controls the “squeezing” in the center, while the parameter β controls the deepest value of l_d . Notice that β is chosen as the solution of $l_d(y_{min}) = \frac{y_{min}}{2}$ but not at y_{min} : it is the solution giving the best accuracy after multiple tries.

Figure 5 compares the logarithmic discretization to the uniform discretization. As expected, the behavior with the former leads to fewer points close to y_{min} and more points close to y_{max} . Note also the higher density of points close to $y = 0$.

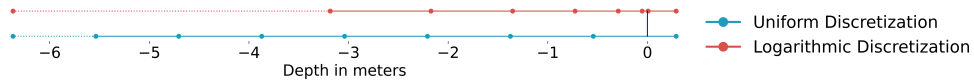


Figure 5. This figure shows a comparison between a **uniform discretization in blue** and a **logarithmic discretization in red**. The dotted parts represent the last interpolation toward a null velocity at y_{min} .

Moreover, using the logarithmic distribution leads to $l_d(y_{min}) = \frac{y_{min}}{2}$. Assuming that the velocity at y_{min} is null, then for any depth between y_{min} and $\frac{y_{min}}{2}$ the velocity can be computed between the one at $\frac{y_{min}}{2}$ and 0.

Figure 6 compares the accuracy using linear mechanism and the exponential interpolation with the logarithmic discretization. Clearly the latter gives much better accuracy, as expected.

3.6.3. Choosing the interpolation degree

Knowing the interpolation method, the interpolation degree d (number of points in the table) must be decided. Note, that using more points results in better accuracy, but also more computation time. Then, a trade-off between performance and accuracy must be determined. With this aim, the *multi-objective optimization* method is used.

Briefly, this method reduces a multi-criteria optimization problem into a one dimensional one. It defines a one dimensional function as a linear sum of different objective functions; here, it concerns the performance and accuracy for a given interpolation degree.

Hence, this optimization function J is defined as follows:

$$J(d) = \alpha P(d) + \beta A(d) \quad (28)$$

where d is the interpolation degree, $P(d)$ measures the performance of the velocity interpolation, $A(d)$ measures the accuracy of the velocity interpolation, and α and β are the weight arbitrary assigned to the performances and the accuracy functions.

To make $P(d)$ and $A(d)$ having the same order of magnitude, the units are the **seconds** for performance and the **meter per seconds** for accuracy (see figure 7). More-

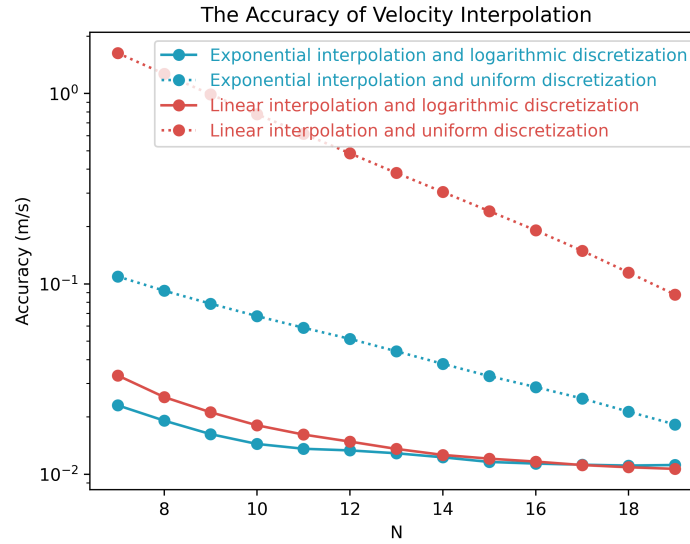


Figure 6. This figure represents the accuracy of different type of interpolation in function of the size of the discretization N . The accuracy axis used a logarithmic scale to be more readable. It uses 10000 positions from a continuous uniform distribution in the parallelepiped $[-1000, 1000] \times [-125, 4.5] \times [-1000, 1000]$ and with a wind speed of 20 m.s^{-1} . The interpolated velocity $\tilde{\mathbf{v}}$ and the analytical velocity \mathbf{v} are evaluated. The accuracy is defined by the mean of all positions of $|||\tilde{\mathbf{v}}| - |\mathbf{v}|||$. It can be noticed that considering a uniform discretization, then exponential interpolation has a better accuracy than linear one. Logarithmic discretization is much better than uniform discretization, whatever the used interpolation. At least, for low N , exponential interpolation gives slightly better result than linear interpolation.

over, the performance being the more important for real-time process, the following arbitrary choice are made for the coefficients of J : $\alpha = 10$ and $\beta = 2$.

Figure 8 shows the function J using these parameters. It appears that its minimum is obtained with $d = 8$. It is the value used in the Arc Blanc framework.

3.7. Coupling solid and fluid

The physical simulation based on the Tessendorf's method is very fast, and the spectrum approach leaves a lot of control to the user. However, it doesn't simulate the interaction between the fluid and a solid, which is needed for adding some boats in the simulation. To overcome this flaw, the Arc Blanc framework uses two methods: a first one for fluid-to-solid action, and a second one for solid-to-fluid action.

These two methods are designed with the following constraints in mind:

1. Rely on simple parameterization for non-physicists, to be easily usable by artists;

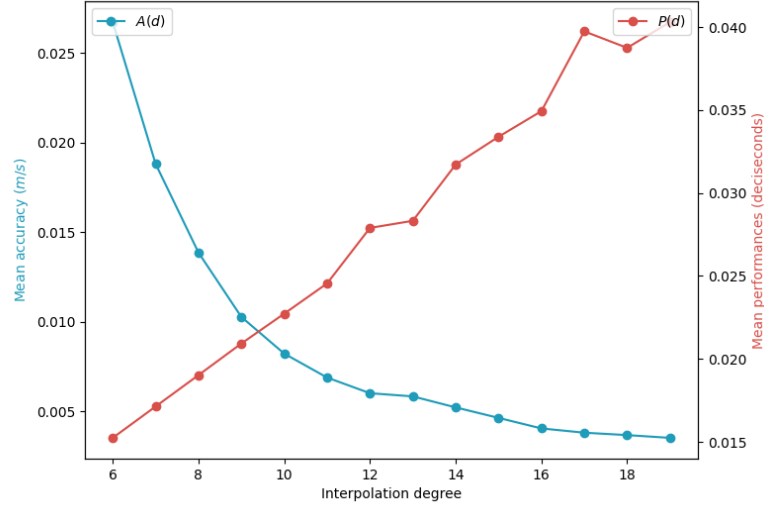


Figure 7. These figures represent the different objective for choosing the interpolation degree. In blue, the mean accuracy of velocity interpolation in meters per seconds, we denote this function $A(d)$. In red, the mean performances of velocity interpolation in deciseconds, we denote this function $P(d)$. We estimate this function with 10000 sample.

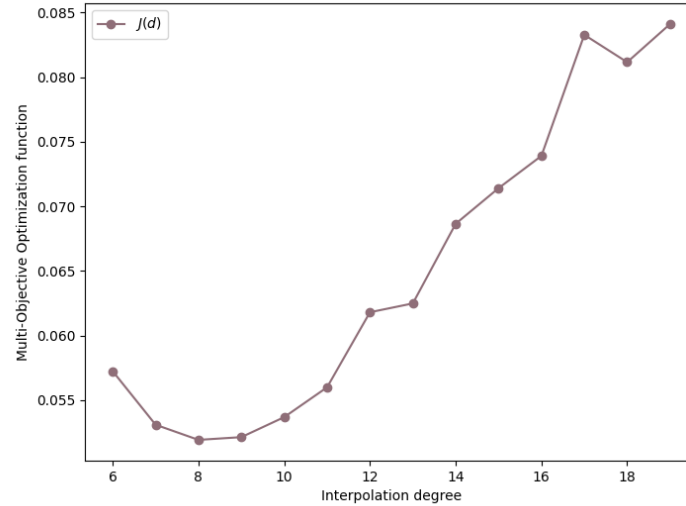


Figure 8. Multi-objective function P to optimize, with two objectives: performance and accuracy. Its minimum is reached by the interpolation degree of 8. For more details on each objective, see Figures 7 which represent them individually.

2. Not requiring too many pre-calculations, to avoid an overly complex framework;
3. Have excellent performance (a few milliseconds at most), so that the Arc Blanc framework reaches real time globally, including all simulation and rendering stages.

4. Fluid-to-solid action

The action of the fluid on a given solid can be approximated by a *set of forces* acting continuously on the *contact surface* between the fluid and the solid. In the Arc Blanc framework, the contact surface is represented using the triangulation of the solid's mesh, leading to a discrete approximation of the set of forces. Moreover, to remain real-time the Arc Blanc framework uses forces computed from simple geometric and physical parameters only. To maintain realistic physics after these discrete approximations and those described in subsequent sections, it is important to use a closed mesh, uniformly triangulated. In addition, for meshes representing vessels, ensuring symmetry is crucial to maintain stability.

4.1. Geometrical Parameters

In the Arc Blanc framework, the forces are computed for each boat or body, independently of the others. The calculation of the forces needs the following geometrical data from a body and the water surface: the lower hull (part of the hull in the water), the waterline, and the upper hull (part of the hull above the water).

At first, the Arc Blanc framework checks the vertical position of body's each vertex relative to the water surface. Then, it assigns a status to each body's face: submerged, partially submerged or not submerged. The triangles that are partially submerged are divided as done in Kerner (2016) [Kerner], producing the waterline as the intersection edges between the mesh and the water surface. This waterline is used later to compute the mask in Section 5.4. Then the body surface is decomposed into a set $\{T_i^s\}$ of submerged triangles, and $\{T_i^{ns}\}$ of not submerged ones. The Arc Blanc framework computes the area of each submerged or not submerged triangle at this step too.

The buoyancy calculation presented in Section 4.2.1 requires the full submerged volume v_w of the mesh. The Arc Blanc framework uses the prism approximation similarly to the approximation proposed by Bajo *et al.* (2020) [Bajo et al.]. While Bajo *et al.* compute the submerged volume at the texel level, the same principle can be applied using triangles instead of texels using as they did the divergence theorem. Specifically, v_w is approximated as the sum of the prisms with bases corresponding to the triangle areas A_i and heights defined by the distance d_i between the triangle centers p_i and the water surface $h(p_i, t)$. Each term in the sum is weighted by the

vertical component of the triangle normal n_i^y :

$$v_w = \sum_{T_i^s} A_i d_i n_i^y. \quad (29)$$

Note that this formula is correct only under the assumption that the mesh is closed.

The pseudocode for the all geometrical calculations performed in this section can be read in the Algorithm 2.

Algorithm 2 Computation of Geometrical Parameters

Require: List of triangles T_i with vertex positions \mathbf{v}_i and normal \mathbf{n}_i

- 1: **for** each triangle $T_i = (\mathbf{v}_0, \mathbf{v}_1, \mathbf{v}_2)$ with normal \mathbf{n}_i **do**
- 2: Retrieve water height d_0, d_1 , and d_2 at vertices $\mathbf{v}_0, \mathbf{v}_1$, and \mathbf{v}_2
- 3: Compute area: $A_i = \frac{1}{2} \|(\mathbf{v}_1 - \mathbf{v}_0) \times (\mathbf{v}_2 - \mathbf{v}_0)\|$
- 4: Compute centroid: $\mathbf{p}_i = \frac{1}{3}(\mathbf{v}_0 + \mathbf{v}_1 + \mathbf{v}_2)$
- 5: Compute centroid depth: $d_i = \frac{1}{3}(d_0 + d_1 + d_2)$
- 6: **if** $d_0 \geq 0$ and $d_1 \geq 0$ and $d_2 \geq 0$ **then** // Fully above water
- 7: Set submerged area $A_i^s = 0$
- 8: Set volume contribution $v_{w_i} = 0$
- 9: **else if** $d_0 < 0$ and $d_1 < 0$ and $d_2 < 0$ **then** // Fully submerged
- 10: Set submerged area $A_i^s = A_i$
- 11: Compute submerged volume: $v_{w_i} = A_i d_i n_i^y$
- 12: **else if** one vertex is above the water surface (e.g., $d_0 \geq 0$) **then** // Partially submerged
- 13: Compute intersection points $\mathbf{p}_1, \mathbf{p}_2$ using linear interpolation:
- 14: $\mathbf{p}_j = \mathbf{v}_j + \alpha(\mathbf{v}_k - \mathbf{v}_j)$ where $\alpha = \frac{d_j}{d_j - d_k}$
- 15: Compute submerged area A_i^s from new submerged sub-triangle(s)
- 16: Compute submerged volume: $v_{w_i} = A_i^s d_i n_i^y$
- 17: **else if** two vertices are above the water surface (e.g., $d_0 \geq 0, d_1 \geq 0$) **then** // Mostly submerged
- 18: Compute intersection points $\mathbf{p}_1, \mathbf{p}_2$ using linear interpolation
- 19: Compute submerged area A_i^s from the remaining submerged sub-triangle
- 20: Compute submerged volume: $v_{w_i} = A_i^s d_i n_i^y$
- 21: **end if**
- 22: **end for**

At last, from all the submerged faces T_i^s the Arc Blanc framework computes the center of immersion c_i used for the buoyancy calculation as presented in Section 4.2.

4.2. Forces

The Arc Blanc framework uses three forces as in Kellomaki (2014) [Kellomäki]:

1. Buoyancy \mathbf{F}_b ;
2. Water drag \mathbf{F}_w ;
3. Air drag \mathbf{F}_a .

These forces are computed for each triangle of the lower or upper hull, and so after the different geometric parameters being calculated.

4.2.1. Buoyancy

The buoyancy is computed once for the whole boat from the following analytical formula:

$$\mathbf{F}_b = -v_w \rho_w \mathbf{g}, \quad (30)$$

where v_w is the submerged volume in m^3 (cf. Section 4.1) and ρ_w is the water density. The water density is obtained at any depth by linear interpolation using the measure of the International Towing Tank Conference (ITTC) [ITTC]. The buoyancy is applied to the center of immersion c_i .

4.2.2. Drag Forces

The Arc Blanc framework calculates drag forces based on the relative velocity between the fluid medium (water or air) and the submerged or exposed portion of the body. This approach is inspired by previous works [Yuksel; Kellomäki; Kerner].

The drag force for each triangle T_i of the body is computed as:

$$\mathbf{F}_d = -\frac{1}{2} C_d \rho A_i^\perp \|\mathbf{v}_{i_{\text{rel}}}\| \mathbf{v}_{i_{\text{rel}}}, \quad (31)$$

where:

- $\mathbf{v}_{i_{\text{rel}}} = \mathbf{v}_i - \mathbf{v}_i^m$ is the relative velocity in $m.s^{-1}$ of the triangle T_i , equal to the difference between its velocity \mathbf{v}_i and the velocity \mathbf{v}_i^m of the fluid medium (water or air) at its center;
- A_i^\perp is the projected area in m^2 of the triangle T_i with respect to the relative velocity unit direction (*i.e.* the vector $\mathbf{v}_{i_{\text{rel}}} / \|\mathbf{v}_{i_{\text{rel}}}\|$);
- ρ is the density of the fluid medium in $kg.m^{-3}$ (ρ_w as defined in Section 4.2.1 for water and $1.204 kg.m^{-3}$ for air⁷);
- C_d is the drag coefficient of the body in the fluid medium, specified by the user.

For the submerged part $\{T_i^s\}$, the medium is water, while for the exposed part $\{T_i^{\neg s}\}$, the medium is air.

⁷According to the international standard atmosphere, the air density at sea level for 20°C is $1.204 kg.m^{-3}$ cf. <https://www.digitaldutch.com/atmoscalc/table.htm>

4.3. Fluid-to-solid algorithm

To ensure a structured and efficient data workflow on the GPU, all computations for a given mesh are performed separately, avoiding data interleaving between different meshes. Each kernel invocation processes a single mesh, iterating over its triangles before moving to the next mesh.

Firstly, for each triangle in the mesh, the geometric parameters are calculated and then used to compute the drag forces. These include necessary attributes such as the submerged volume, normal vectors, and the drag forces acting on submerged and non-submerged parts.

Once per-triangle computations are completed, the forces and geometrical parameters must be integrated into the physics solver, which operates on the CPU. To minimize data transfers and reduce latency, a parallel reduction kernel is applied on the GPU for each mesh individually. This step aggregates all per-triangle forces and parameters into global values for the entire mesh.

Buoyancy, however, is handled differently. Since it depends solely on the total submerged volume rather than individual triangles, it is computed separately using an analytical formula and applied directly at the submerged center without requiring per-triangle summation.

With all global parameters computed, the final step transfers the data to the CPU, where the physics solver integrates the buoyancy and the water drag forces are applied on the submerged center, while air drag forces are applied at the center of the non-submerged part.

This pipeline is presented in Algorithm 3.

A summary of the forces applied to the solid is shown in Figure 9.

5. Solid-to-fluid action

The Arc Blanc framework relies on the method developed by Cords and Staadt (2009) [Cords and Staadt] to simulate the action of the solid on the fluid. The simulation of this action is 3-dimensional by nature. However, it has to be simplified to satisfy the third requirement of Section 3.7, concerning computation time performance. As for fluid simulation in Section 3, the Arc Blanc framework assumes that the interaction from a solid to the fluid can be simulated as a 2D height field. Furthermore, it considers a single frequency for the waves generated by a solid M . These specific waves are called interactive waves. These approximations may seem too strong, but as mentioned above, they are necessary to satisfy the requirements defined in Section 3.7.

Hence, the Arc Blanc framework assumes that the interactive waves are solutions of the following 2D wave equation:

$$\Delta h(\mathbf{x}, t) - \frac{1}{c^2} \frac{\partial^2 h(\mathbf{x}, t)}{\partial t^2} = 0 \quad (32)$$

Algorithm 3 Fluid-to-Solid Interaction Algorithm

```

1: for each mesh do                                     // Iterate over all mesh
2:   for all triangles  $T_i$  do                             // Iterate over all triangles
3:     Compute geometrical parameters                     // Algorithm 2
4:   end for
5: end for
6: for each mesh do                                     // Iterate over all mesh
7:   for all triangles  $T_i$  do                             // Iterate over all triangles
8:     Compute drag forces  $\mathbf{F}_d$  for each triangles      // Section 4.2.2
9:   end for
10: end for
11: for each mesh do                                     // Iterate over all mesh
12:   for all triangles  $T_i$  do                             // Iterate over all triangles
13:     Apply parallel reduction to aggregate forces and geometrical parameters.
14:   end for
15: end for
16: for each mesh do                                     // Iterate over all mesh
17:   Transfer reduced forces and parameters to the CPU
18:   Compute buoyancy force  $\mathbf{F}_b$  from geometrical parameters // Section 4.2.1
19:   Integrate total forces and moments in the physics engine
20: end for

```

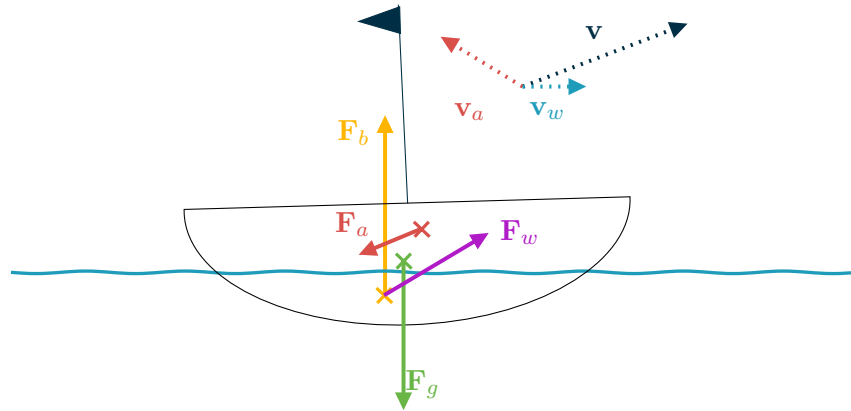


Figure 9. Summary of forces calculation. Using the same notation as Section 4.2 it follows: the buoyancy force F_b in yellow, applied to the center of immersion; the sum of water drag force F_w in purple, applied to the center of immersion too; the sum of the air drag forces F_a in red, applied to the center of the non-submerged part; and finally the gravity force F_g in green, applied to the center of gravity. Different velocities are displayed above the ship: the wind velocity v_a in red; the water velocity v_w in blue; and the object velocity v in black.

where $h(\mathbf{x}, t)$ is the height of the water surface at horizontal position \mathbf{x} and time t , $\Delta = \frac{\partial^2}{\partial x^2} + \frac{\partial^2}{\partial z^2}$ is the Laplacian in 2D and c is the wave velocity expressed in $m.s^{-1}$. The Arc Blanc framework uses the following Dirichlet boundary condition:

$$h(\mathbf{x}, t) = 0 \quad \text{on the boundary.} \quad (33)$$

5.1. Finite-difference method

Following Gomez (2000) [Gomez], the Arc Blanc framework uses the FDM with an explicit scheme to numerically solve the equation (32). It uses a square simulation zone Z of dimension $L \times L$ around a given mesh M . This zone is regularly discretized with a δ step. Time is also regularly discretized with a time step dt .

In the FDM simulation, the Arc Blanc framework denotes by $h_{i,j}^n$ the water height $h(i \times \delta, j \times \delta, n \times dt)$ for discrete location $(i, j) \times \delta$ and time $n \times dt$. This leads to the following explicit scheme:

$$h_{i,j}^{n+1} = a (h_{i+1,j}^n + h_{i-1,j}^n + h_{i,j+1}^n + h_{i,j-1}^n - 4h_{i,j}^n) + 2h_{i,j}^n - h_{i,j}^{n-1} \quad (34)$$

where

$$a = \frac{c^2 dt^2}{\delta^2}. \quad (35)$$

The Dirichlet boundary condition gives $h_{i,j}^n = 0$ for i or j being on the boundary of Z . Since a new wave is generated at each time step, a damping effect is added to make them disappear gradually. Hence, the right part of Equation (34) is multiplied by the **damping factor** $d(t) = d^n$.

This damping factor is linearly related to the velocity of the mesh $\mathbf{v}_M(t)$ to ensure numerical stability and is defined as:

$$u = \text{clamp} \left(\frac{\|\mathbf{v}_M(t)\|}{v_{max}}, 0, 1 \right),$$

$$d(t) = \text{lerp}(d_0, d_{max}, u), \quad (36)$$

where:

- $\text{clamp}(x, 0, 1)$ limits the value of x to the range $[0, 1]$;
- $\text{lerp}(a, b, t) = (1 - t)a + tb$ is the linear interpolation function;
- v_{max} is the velocity threshold, above which the damping factor equals its maximum value d_{max} ;
- d_0 is the damping value for a null velocity.

For a plausible appearance, the Arc Blanc framework uses the following values by default:

$$\begin{cases} d_0 &= 0.98, \\ d_{max} &= 0.999, \\ v_{max} &= 5m.s^{-1}. \end{cases} \quad (37)$$

Nevertheless, the user can adjust these values in a way that a body M causes more or less interaction waves.

5.2. Grid translation

The waves generated by a given body M are defined in its local coordinates system. Hence, when M moves, the waves have to move accordingly as done by Cords and Staadt (2009) [Cords and Staadt]. A first solution consists of applying the translation to the grid at times t and $t - dt$ and then of using the integration scheme of Equation (34). Nevertheless, these time-consuming shifts can be avoided by using the following domain translation:

$$\begin{cases} k = i - \left\lfloor \frac{\mathbf{p}_x(t+dt) - \mathbf{p}_x(t)}{\delta} \right\rfloor \\ l = j - \left\lfloor \frac{\mathbf{p}_z(t+dt) - \mathbf{p}_z(t)}{\delta} \right\rfloor \\ o = i - \left\lfloor \frac{\mathbf{p}_x(t+dt) - \mathbf{p}_x(t-dt)}{\delta} \right\rfloor \\ p = j - \left\lfloor \frac{\mathbf{p}_z(t+dt) - \mathbf{p}_z(t-dt)}{\delta} \right\rfloor \end{cases} \quad (38)$$

where $\mathbf{p}(t) = [p_x(t) \ p_z(t)]^T$ is the position of the mesh M at time t , k and l (respectively o and p) are the shifted indices (see Figure 10) defined by the translation of M at times $t+dt$ from times t (respectively from times $t-dt$). Then, the integration scheme can be rewritten as follows:

$$h_{i,j}^{n+1} = d^n (a (h_{k+1,l}^n + h_{k-1,l}^n + h_{k,l+1}^n + h_{k,l-1}^n - 4h_{k,l}^n) + 2h_{k,l}^n - h_{o,p}^{n-1}) \quad (39)$$

Since M moves, the shift indexes k , l , o , and p can be outside the boundary of the simulation zone Z . To solve this problem, the size m of the boundary of Z is increased such that $m > 1$ (see Figure 11). The Arc Blanc framework takes $m = 16$ which is large enough for large translations.

To ensure high performance, the FDM update step is executed entirely on the GPU, with a single kernel processing all vertices of the FDM grid in parallel. Each thread updates one grid point, significantly reducing computation time. The pseudocode associated to this method is shown in Algorithm 4.

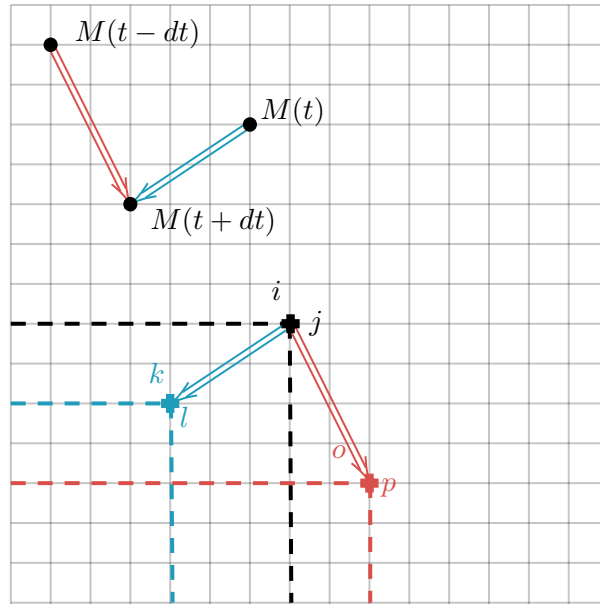


Figure 10. An example of the relationship between the indices (i, j) , (k, l) , and (o, p) in the finite-difference method grid translation, showing how the grid indices are affected by the motion of the body M at different time steps t , $t - dt$, and $t + dt$

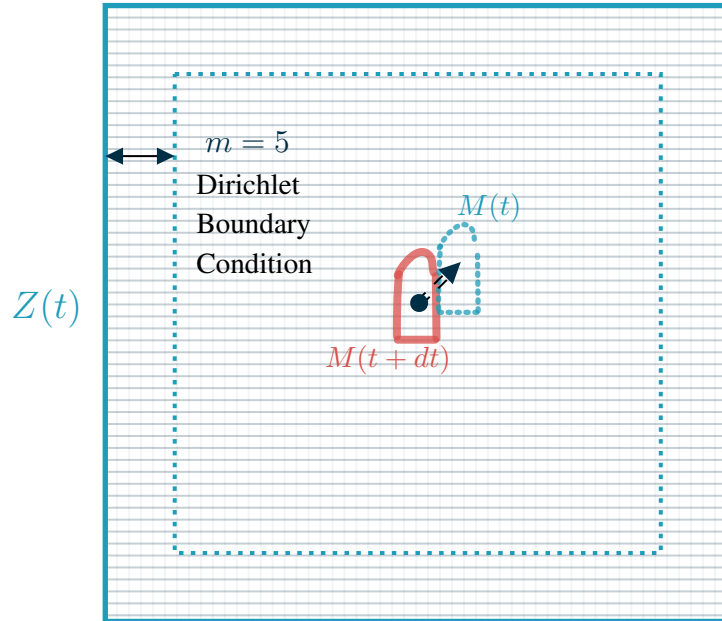


Figure 11. An example of zone $Z(t)$ at a time t using boundary size $m = 5$. In dotted blue the mesh M at time t . In red the same mesh at time $t + dt$.

Algorithm 4 FDM Algorithm

Require: List of zone-specific parameters: $a, b, d(t), \mathbf{p}(t - dt), \mathbf{p}(t)$ and $\mathbf{p}(t + dt)$.

- 1: **for** each vertices of the FDM grid i, j and zone Z in the simulation domain **do**
- 2: $k = i - \left\lfloor \frac{\mathbf{p}_x(t+dt) - \mathbf{p}_x(t)}{\delta} \right\rfloor$
- 3: $l = j - \left\lfloor \frac{\mathbf{p}_z(t+dt) - \mathbf{p}_z(t)}{\delta} \right\rfloor$
- 4: $o = i - \left\lfloor \frac{\mathbf{p}_x(t+dt) - \mathbf{p}_x(t-dt)}{\delta} \right\rfloor$
- 5: $p = j - \left\lfloor \frac{\mathbf{p}_z(t+dt) - \mathbf{p}_z(t-dt)}{\delta} \right\rfloor$
- 6: $h_{i,j}^{n+1} = d \cdot (a \cdot (h_{k-1,l} + h_{k+1,l} + h_{k,l-1} + h_{k,l+1}) + b \cdot h_{k,l} - h_{o,p}^{l-1})$
- 7: **end for**

5.3. Stability

The stability of the scheme defined by Equation (39) is related to the CFL condition (for Courant–Friedrichs–Lewy), here given as follows:

$$\frac{c^2 dt^2}{\delta^2} \leq 0.5 \quad (40)$$

The parameter dt is considered fixed throughout the simulation. One contribution of this article is to adapt the simulation's parameters c and δ to the CFL, as presented below.

Preliminary tests have shown that δ must be small for a low velocity $\mathbf{v}_M(t)$ of M . Moreover, δ must be large enough for Z to encompass M and the waves generated by M . The size of M is defined from its bounding box (b_x, b_y, b_z) as $S(M) = \max(b_x, b_z)$. The Arc Blanc framework lets the user define the bounds δ_{min} and δ_{max} so that Z is at least twice as large as M . Then δ is defined as follows:

$$\delta = \begin{cases} 0.999 \, dt & \text{if } \|\mathbf{v}_M(t)\| < 1 \\ \|\mathbf{v}_M(t)\| 0.999 \, dt & \text{if } \|\mathbf{v}_M(t)\| \geq 1 \end{cases} \quad (41)$$

Finally δ is clamped between δ_{min} and δ_{max} . The value of c is deduced from δ and dt to ensure that the inequality in Equation 40 is always satisfied:

$$c = \sqrt{0.49} \frac{\delta}{dt}. \quad (42)$$

This choice of c ensures numerical stability.

5.4. Wave generation

While the FDM allows to simulate the propagation of the interactive waves, one more input is required for the wave generation: an alteration of the free surface of the height map. The Arc Blanc framework uses a new way to compute this input, which provides

a satisfying result no matter the form of the body generating the waves. The input of the FDM is called **mask**.

The idea behind the mask is to distort the grid of the FDM by reproducing the intersection surface between M and the free surface. Here, free surface refers to the ambient waves of Tessendorf's method (see Section 3) plus the interactive waves generated by all solids except M . It does **not** include the free surface generated by M , or the simulation would face a divergence issue.

This intersection has already been computed as part of the geometric parameters in Section 4.1. It is given as a list of 3D points forming the intersection polygons of the hull with the free surface. These points are moved from the world coordinates system to the one of Z , the surrounding grid of M .

Hence, for a body M the wave generation relies on two different steps: First, a mask is defined from this list of 3D points, corresponding to the vertices of Z contained in one intersected polygons. Second, the height h of each point in the mask is determined using an ad hoc function. These two steps are detailed in the following two sections.

5.4.1. Calculate the mask

The FDM needs the height of the vertices below the body. This is computed from the mask, composed of the vertices of Z contained in one of the intersections polygons at least. This is done using the **Point in Polygon** strategy described in Haines (1994) [Haines].

The principle of this algorithm is as follows: for each vertex v of the grid Z , a ray starting at v and with direction z is generated, and its number of intersection with all the intersection polygons is computed. v is in the polygon if this number of intersections is odd; otherwise it is not.

To ensure consistency regardless of the body's orientation, a rotation alignment is applied to the intersected polygons before processing.

To reduce the computation times, this strategy is applied to the vertices v included into the bounding box of the intersections polygons. Since the number of vertices v of Z is at least twice as the size of M , this simple method reduces efficiently the number of ray to polygon calculations.

5.4.2. Evaluate the height of vertices in the mask

Knowing all the vertices in the mask, their height must be given as input of the FDM. The Arc Blanc framework uses a simple model that tries to reproduce parts of the idea of Cords and Staadt (2009) [Cords and Staadt]. By construction of the grid Z , M has its bow oriented on the positive side of the z axis, and its starboard (right-hand side when facing the bow) on the positive side of the x axis. Hence, h is made such that from the vertex at position \mathbf{x} , the front of the mask is above the free surface and the back below, in a way that is proportional to the speed of M . Moreover, the boat forms

a V shape laterally, with its center a bit below the extremity of the side. Figure 12 presents the desired shape from three different perspectives.

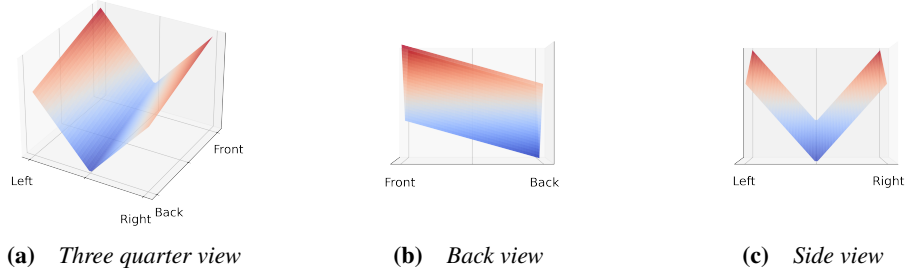


Figure 12. Three different theoretical point of view of the mask for a simple rectangle.

To simplify, $h(\mathbf{x})$ is defined as the sum of two orthogonal functions $f(x)$ and $g(z)$, where $f(x)$ represent the side effect, and $g(z)$ the front/back effect.

The function f models the side effect using a shape in V . It is defined as follows:

$$f(x) = \frac{|x - c_x|}{b_x}. \quad (43)$$

The V -shape is obtained from the absolute value of the abscissa x shifted to the center c_x of M . The amplitude of the height is controlled by the inverse of the bounding box size b_x of M on the x axis.

The purpose of g is to shift up the front of the interactive wave and shift down its back. The idea is that a moving body displaces the water from its submerged hull, producing a high interactive wave in front of the body. This effect is modeled using a quite simple affine function $g(z) = a \cdot z + b$. The slope coefficient a is defined considering the maximum height h_b on the back of the mask and the height h_f on its front.

While h_b is defined by the user, the value of h_f is estimated as follows:

$$h_f = \|\mathbf{v}_M\| h_M \times i_f \times \frac{v_w}{v_M}, \quad (44)$$

where \mathbf{v}_M is the velocity of the body M , h_M is the full height of M , i_f is a user parameter allowing more user control, v_w is the submerged volume of M (see Section 4), and v_M is the full volume of M . Hence, for more realism h_f is made proportional to the velocity of M : the faster M moves, the bigger the waves generated by M at its front are.

The values of a and b are straightforward to obtain by considering the height at the back and the front, so using the relations $g(z_{min}) = h_b$ and $g(z_{max}) = h_f$, where z_{min} is the z -coordinates of the back and z_{max} the z -coordinate of the front. From the first relation, it comes $b = h_b - a \cdot z_{min}$. From the second, it comes $a = (h_f - h_b) / b_z$,

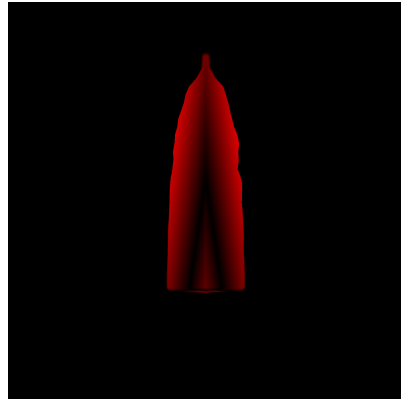
where $b_z = z_{max} - z_{min}$ is the bounding box extend in z axis. This allows to simplify the term b as $b = (h_b z_{max} - h_f z_{min}) / b_z$.

The functions $f(x)$ and $g(z)$ are then used to obtain the height of the mask as follows, but using the user factor b_w to allow more user control:

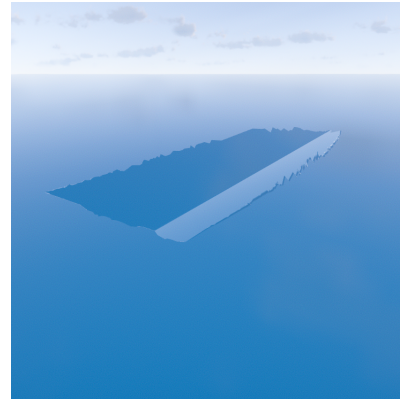
$$h(\mathbf{x}) = b_w (f(x) + g(z)). \quad (45)$$

Note that h is only well-defined if the bow of M is oriented on the positive z axis. Therefore, a 2D rotation is first applied to the vertices \mathbf{x} before applying h .

Figure 13 shows some views of the application of this interactive waves process.



(a) The height of the mask of a simple boat encoded in a single channel texture.



(b) The height of the mask of a simple boat in a 3D scene with a very low sea state. Boat rendering and wave propagation has been disabled to only display the initial step of the height of the mask.

Figure 13. Two different views of the height of the mask defined by Equation 45 for a simple boat.

The mask calculation is implemented on the GPU to leverage parallel processing efficiency. A dedicated kernel is launched for each zone only for the vertices of the FDM grid that fall within the bounding box of the intersection polygon, reducing computational overhead. Each thread independently performs the point-in-polygon test using a ray-intersection method and determines whether the corresponding vertex should be included in the mask. Once identified as inside an intersection polygon, the height function is applied per vertex, using the predefined wave generation model. The full process is detailed in Algorithm 5.

6. Results and discussions

Sections 3, 4 and 5 describe three methods to handle the main parts of an ocean simulation: the free surface, and the coupling between a solid and a fluid. Each

Algorithm 5 Mask Calculation via Point-in-Polygon Test

Require: The bounding box, the intersection polygon

```
1: for each vertices of the FDM grid  $i, j$  within the bounding box in a zone  $Z$  do
2:    $counter \leftarrow 0$  // Initialize the counter for intersections
3:   for each edges  $(v_k, v_{k+1})$  of the intersection polygon do
4:      $p_1 = (i, j)$ 
5:      $p_2 = (i + \infty, j + \infty)$ 
6:      $p_3 = v_k$ 
7:      $p_4 = v_{k+1}$ 
8:     if Segment-Intersect( $p_1, p_2, p_3, p_4$ ) do then
9:        $counter++ = 1$ 
10:    end if
11:  end for
12:  if  $counter \bmod 2 = 1$  then // Point  $(i, j)$  is inside an intersection polygon.
13:     $h_{i,j}^n = b_w(f(x) + g(z))$  // See Equation 45
14:  end if
15: end for
```

method has been chosen to find the best ratio between high performance and physics accuracy.

Notice that each method interacts naturally with the two others, as shown in Figure 14. Indeed, Tessendorf's method generates the free surface. As depicted by arrow (0), the free surface method impacts the force calculation of the fluid-to-solid method. The force calculation of the fluid-to-solid method impacts the mask calculation (arrow (1)), which is the input of the solid-to-fluid method. The solid-to-fluid method modifies the free surface around the solid and is an input of the ocean waves simulation (arrow (2)). All these interactions loops through the simulation over time. As a result, the three components of the Arc Blanc framework have an impact on the two others (arrows (3), (4) and (5)) at the next time-step. For example, since the solid-to-fluid method impacts the free surface (arrow (2)), and the free surface impacts the force calculation used in the fluid-to-solid (arrow (0)), then indirectly the solid-to-fluid method has an indirect impact on the fluid-to-solid action (arrow (3)).

Two experiments with different solids have been conducted to demonstrate the efficiency of the Arc Blanc framework. These experiments ran on a [Intel Core i7-10700](#) and a [Nvidia GeForce RTX 2070 Super](#) using single-precision floating-point numbers. The ocean was simulated with three cascades using a resolution of 256×265 . Moreover, the resolution of FDM grids is set to 512×512 .

The first experiment called *one-solid* simulates a single solid corresponding to a motorboat. This motorboat is running in the scene. Its model is composed of 165 triangles for the simulation. Two captures of *one-solid* can be seen in the top row of

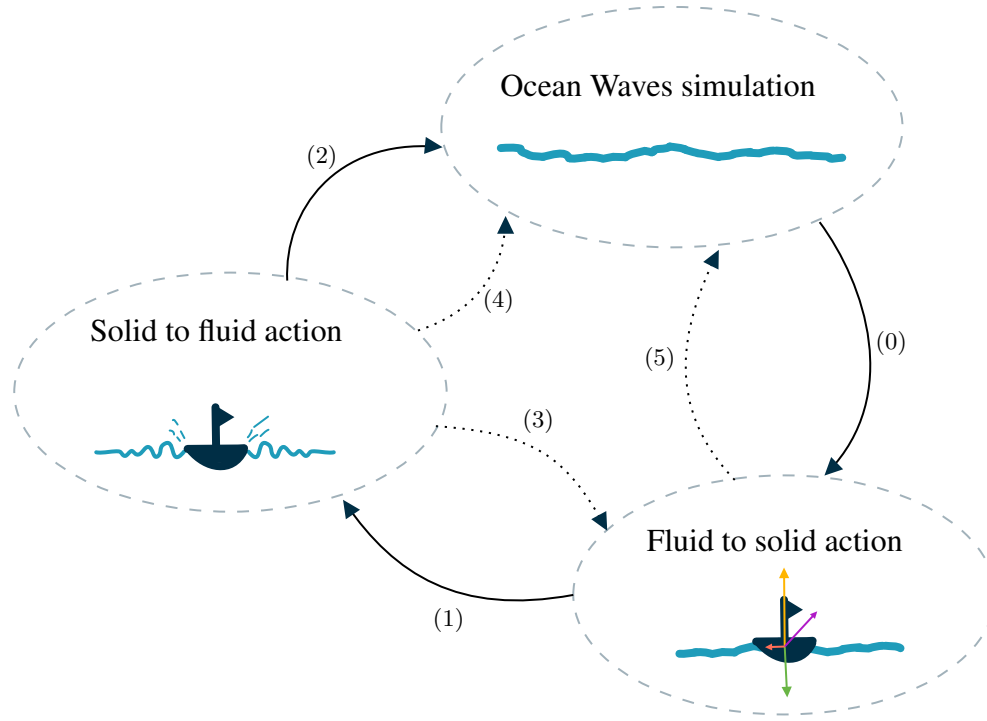


Figure 14. Interactions between the ocean waves simulation (Section 3), the fluid-to-solid method (Section 4) and the solid-to-fluid method (Section 5). The arrow represents an interaction between two methods. The arrow direction indicates that the method from which the arrow originates impacts the method to which the arrow is pointing to.

Figure 15. The sea-state is 1 on the Beaufort scale on Figure 15a, leading to a very calm sea. Hence, the interaction waves appear clearly behind the motorboat. On the contrary, the sea-state is 6 for Figure 15b, leading to big waves and almost completely hiding interaction waves.

The second experiment called *ten-solids* simulates ten solids. It extends the first experiment as follows:

- 1 sailing boat with a mesh made of 270 triangles.
- 2 yachts with a mesh made of 146 triangles.
- 6 zodiacs with a mesh made of 568 triangles.

This makes a total of 4135 triangles. Each of these ten solids uses its own grid for the solid to fluid coupling FDM. Two captures of the second experiment can be seen in the bottom row of Figure 15. The sea state is 1 for Figure 15c where again small interaction waves can be seen for the motorboat (the others are not propelled). On



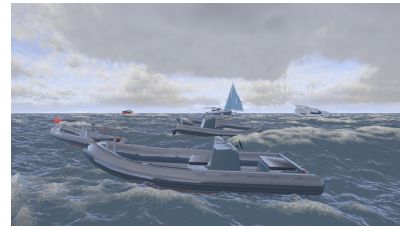
(a) One-solid using sea state 1.



(b) One-solid using sea state 6.



(c) Ten-solids using sea state 1.



(d) Ten-solids using sea state 4.

Figure 15. The two experiments with different sea state: *one-solid* on top row, and *ten-solids* on bottom one.

Figure 15d the sea state is set to 4, leading to relatively big waves. Using 10 boats and so FDM grids does not impact too much the computation times, as seen below.

Table 16 shows a summary of GPU computation times for each method and with these two experiments. As detailed in previous sections, all heavy computations in the Arc Blanc framework are offloaded to the GPU, while the CPU is minimally involved in physical calculations. This design choice ensures that the CPU remains available for other standard game or simulation tasks, optimizing overall system performance. Therefore, CPU computation times are not considered, as they are negligible compared to GPU ones. First, it can be observed that real-time performance is largely achieved, even with *ten-solids*. One of the most computationally intensive steps is geometry computation, which presents an opportunity for further optimization. A closer inspection suggests that refining memory access patterns and minimizing warp branch divergence in the GPU kernel could enhance performance and efficiency. Besides, as most of the computations are performed on the GPU, it can be observed that computation times do not grow linearly with the number of solids. Indeed, the Arc Blanc framework processes each solid and each FDM grid simulation in parallel.

		XP 1 (one-solid)	XP 2 (ten-solids)
Tessendorf's method (§ 3)	Height (§ 3.1)	0.376	0.376
	Velocity (§ 3.4)	1.175	1.175
	Total	1.551	1.551
Fluid-to-solid coupling (§ 4)	Geometry (§ 4.1)	1.125	4.588
	Forces (§ 4.2)	0.406	3.677
	Total	1.531	8.265
Solid-to-fluid coupling (§ 5)	FDM (§ 5.1)	0.100	0.831
	Mask (§ 5.4)	0.238	1.656
	Total	0.338	2.487
Total		3.414	12.297

Figure 16. GPU computation times in milliseconds for the main parts of the Arc Blanc framework. Only GPU execution times is shown, as CPU ones are negligible.

7. Conclusions

This article presents three methods that together produce a realistic albeit approximate simulation of the ocean, and the way used to combine them together. These methods are simple to implement and fully parallelizable on GPU. The Arc Blanc framework is a demonstration that these methods achieve real-time performance on a desktop PC (see section 6).

This article gives an original expression for the ocean velocity associated with the Tessendorf method, as well as the key details of its implementation. This velocity is an important input for the realistic calculation of fluid-induced forces on solids. This also improves the stability and physical coherence of the FDM for wave generation.

The two solid/fluid coupling methods are highly efficient, but they present many physical approximations. Hence, to increase the realism of the Arc Blanc framework, future works will include the hybridization of a smoothed particle hydrodynamics (SPH) method for solid/fluid coupling and Tessendorf methods on a larger scale.

Acknowledgements

The first author David Algis has been supported by the [Association nationale de recherche et de technologie \(ANRT\)](#)⁸ and by the [Pôle Image Magélic](#). We would like to thank the colleague of David Algis at Studio Nyx, particularly Jeremy Bois and David Deckeur. Thanks to Naval Group for initiating this project. Finally, we would also like to thank Yannick Privat at the [Institut de recherche mathématique avancée \(IRMA\)](#) which help us on the velocity calculation.

⁸Contract number 2021/1157

References

- AKINCI, N., IHMSEN, M., AKINCI, G., SOLENTHALER, B., AND TESCHNER, M. Versatile rigid-fluid coupling for incompressible SPH. *ACM Transactions on Graphics*, 31(4):62:1–62:8. ISSN 0730-0301. URL: <https://dl.acm.org/doi/10.1145/2185520.2185558>. 73
- BAJO, J. M., PATOW, G., AND DELRIEUX, C. A. Realistic Buoyancy Model for Real-Time Applications. 39(6):217–231. ISSN 0167-7055, 1467-8659. URL: <https://diglib.eg.org/server/api/core/bitstreams/3758e8d3-4161-46c4-abd5-7292009b3523/content>. 87
- BANNER, M. L. Equilibrium spectra of wind waves. *Journal of Physical Oceanography*, 20: 966–984. URL: https://journals.ametsoc.org/view/journals/phoc/20/7/1520-0485_1990_020_0966_esoww_2_0_co_2.xml?tab_body=pdf. 76
- BENDER, J. AND KOSCHIER, D. Divergence-free SPH for incompressible and viscous fluids. *IEEE Transactions on Visualization and Computer Graphics*, 23(3):1193–1206. ISSN 1941-0506. URL: <https://dl.acm.org/doi/10.1145/2786784.2786796>. Conference Name: IEEE Transactions on Visualization and Computer Graphics. 73
- CANABAL, J. A., MIRAUT, D., THUEREY, N., KIM, T., PORTILLA, J., AND OTADUY, M. A. Dispersion kernels for water wave simulation. *ACM Transactions on Graphics*, 35(6):1–10. URL: <https://dl.acm.org/doi/10.1145/2980179.2982415>. Publisher: Association for Computing Machinery (ACM). 74
- CASAS-YRURZUM, S., RUEDA, S., RIERA, J., AND FERNÁNDEZ, M. On the real-time physics simulation of a speed-boat motion. pages 121–128. URL: https://www.researchgate.net/publication/314208045_On_the_Real-time_Physics_Simulation_of_a_Speed-boat_Motion. 73
- CHENTANEZ, N. AND MÜLLER, M. Real-time simulation of large bodies of water with small scale details. In *Proceedings of the 2010 ACM SIGGRAPH/Eurographics Symposium on Computer Animation*, SCA '10, pages 197–206. Eurographics Association. URL: https://www.researchgate.net/publication/220789308_Real-time_Simulation_of_Large_Bodies_of_Water_with_Small_Scale_Details. event-place: Madrid, Spain. 74
- COOLEY, J. W. AND TUKEY, J. W. An algorithm for the machine calculation of complex fourier series. *Mathematics of Computation*, 19(90):297–301. ISSN 0025-5718, 1088-6842. URL: <https://www.ams.org/mcom/1965-19-090/S0025-5718-1965-0178586-1/>. 81
- CORDS, H. AND STAADT, C. Real-time open water environments with interacting objects. *Proceedings of the Fifth Eurographics Conference on Natural Phenomena*, pages 35–42. URL: <https://dl.acm.org/doi/10.5555/2381692.2381697>. ISBN: 9783905674118 Place: Goslar, DEU Publisher: Eurographics Association. 71, 74, 90, 93, 96

- DONELAN, M. A., HAMILTON, J., HUI, W. H., AND STEWART, R. W. Directional spectra of wind-generated ocean waves. *Philosophical Transactions of the Royal Society of London. Series A, Mathematical and Physical Sciences*, 315(1534):509–562. URL: <https://royalsocietypublishing.org/doi/10.1098/rsta.1985.0054>. Publisher: Royal Society. 76
- DUPUY, J. AND BRUNETON, E. Real-time animation and rendering of ocean whitecaps. In *SIGGRAPH Asia 2012 Technical Briefs*, pages 1–3. ACM. ISBN 978-1-4503-1915-7. URL: <https://dl.acm.org/doi/10.1145/2407746.2407761>. 72, 79
- FONSECA, N. AND SOARES, C. G. Time-domain analysis of large-amplitude vertical ship motions and wave loads. *Journal of Ship Research*, 42(2):139–153. ISSN 0022-4502. URL: https://www.researchgate.net/publication/279892381_Time-Domain_Analysis_of_Large-Amplitude_Vertical_Ship_Motions_and_Wave_Loads. 73
- GISSLER, C., PEER, A., BAND, S., BENDER, J., AND TESCHNER, M. Interlinked SPH pressure solvers for strong fluid-rigid coupling. *ACM Transactions on Graphics*, 38(1):5:1–5:13. ISSN 0730-0301. URL: <https://animation.rwth-aachen.de/media/papers/63/2019-TOG-StrongCoupling.pdf>. 73
- GOMEZ, M. Interactive simulation of water surfaces. In DELOURA, M., editor, *Game Programming Gems*, pages 187–194. Charles River Media. ISBN 1-58450-049-2. URL: <https://gameenginegems.com/gemsdb/article.php?id=81>. 73, 74, 92
- HAINES, E. Point in polygon strategies. In *Graphics gems IV*, pages 24–46. Academic Press Professional, Inc. ISBN 978-0-12-336155-4. URL: <https://erich.realtimerendering.com/ptinpoly/>. 96
- HORVATH, C. J. Empirical directional wave spectra for computer graphics. In *Proceedings of the 2015 Symposium on Digital Production*, DigiPro '15, pages 29–39. Association for Computing Machinery. ISBN 978-1-4503-3718-2. URL: <https://doi.org/10.1145/2791261.2791267>. 71, 72, 76, 77
- HULIN, J.-P., GUYON, E., AND PETIT, L. *Hydrodynamique physique*. URL: <https://www.cnrseditions.fr/catalogue/physique-et-astrophysique/hydrodynamique-physique-jean-pierre-hulin/>. 110
- IHMSEN, M., CORNELIS, J., SOLENTHALER, B., HORVATH, C., AND TESCHNER, M. Implicit incompressible SPH. *IEEE transactions on visualization and computer graphics*, 20(3):426–35. URL: <https://ieeexplore.ieee.org/document/6570475>. 73
- ITTC. Fresh water and seawater properties. *ITTC Recommended procedures*. URL: <https://ittc.info/media/4048/75-02-01-03.pdf>. 89, 110
- JESCHKE, S. AND WOJTAN, C. Water wave packets. *ACM Trans. Graph.*, 36(4). ISSN 0730-0301. URL: <https://dl.acm.org/doi/10.1145/3072959.3073678>. Place: New York, NY, USA Publisher: Association for Computing Machinery. 74
- JESCHKE, S., SKŘIVAN, T., MÜLLER-FISCHER, M., CHENTANEZ, N., MACKLIN, M., AND WOJTAN, C. Water surface wavelets. *ACM Transactions on Graphics*, 37(4):1–13. URL: <https://dl.acm.org/doi/10.1145/3197517.3201336>. Publisher: Association for Computing Machinery (ACM). 74

- K. HASSELMANN, T. B. Measurements of wind-wave growth and swell decay during the joint north sea wave project (JONSWAP). *Ergänzungsheft zur Deutschen Hydrographischen Zeitschrift Reihe*, 12:95. URL: https://www.researchgate.net/publication/256197895_Measurements_of_wind-wave_growth_and_swell_decay_during_the_Joint_North_Sea_Wave_Project_JONSWAP. 75
- KELLOMÄKI, T. Rigid body interaction for large-scale real-time water simulation. *International Journal of Computer Games Technology*, 2014:1–12. ISSN 1687-7047, 1687-7055. URL: <http://www.hindawi.com/journals/ijcgt/2014/580154/>. 71, 73, 88, 89
- KERNER, J. Water interaction model for boats in video games: Part 2. URL: <https://www.gamedeveloper.com/programming/water-interaction-model-for-boats-in-video-games-part-2>. 73, 87, 89
- KOSCHIER, D., BENDER, J., SOLENTHALER, B., AND TESCHNER, M. A survey on SPH methods in computer graphics. *Computer Graphics Forum*, 41: 737–760. URL: https://animation.rwth-aachen.de/media/papers/77/2022-CGF-STAR_SPH.pdf. 73
- MOLIN, B. *Hydrodynamique des structures offshore*. Édition Technip. ISBN 978-2-7108-0815-2. URL: <https://hal.science/hal-01320917>. 109
- SALVESEN, N., TUCK, E., AND FALTINSEN, O. Ship motions and sea loads. URL: <https://www.semanticscholar.org/paper/SHIP-MOTIONS-AND-SEA-LOADS-Salvesen-Tuck/6949c72084cd87c27fa6f39eddbc889a13f6b6e5>. 73
- SCHRECK, C., HAFNER, C., AND WOJTAN, C. Fundamental solutions for water wave animation. *ACM Trans. Graph.*, 38(4). ISSN 0730-0301. URL: <https://dl.acm.org/doi/10.1145/3306346.3323002>. Place: New York, NY, USA Publisher: Association for Computing Machinery. 74
- SOLENTHALER, B. AND PAJAROLA, R. Predictive-corrective incompressible SPH. *ACM SIGGRAPH 2009 papers*, pages 1–6. URL: <https://dl.acm.org/doi/10.1145/1576246.1531346>. Conference Name: SIGGRAPH09: Special Interest Group on Computer Graphics and Interactive Techniques Conference ISBN: 9781605587264 Place: New Orleans Louisiana Publisher: ACM. 73
- TEMAM, R. *Navier–Stokes Equations: Theory and Numerical Analysis*, volume 343 of *AMS Chelsea Publishing*. American Mathematical Society. ISBN 978-0-8218-2737-6 978-0-8218-6935-2 978-1-4704-2994-2. URL: <https://www.ams.org/chel/343>. 109
- TESSENDORF, J. eWave: Using an exponential solver on the iWave problem. a. URL: https://people.computing.clemson.edu/~jtessen/reports/papers_files/ewavealgorithm.pdf. 74
- TESSENDORF, J. Gilligan: A prototype framework for simulating and rendering maritime environments. b. URL: https://people.computing.clemson.edu/~jtessen/reports/papers_files/simdoc.pdf. 71, 72, 75

- TESSENDORF, J. Interactive water surface. In *Game Programming Gems 4*, pages 265–274. Charles River Media, c. URL: https://people.computing.clemson.edu/~jtessen/reports/papers_files/Interactive_Water_Surfaces.pdf. 74
- TESSENDORF, J. Simulating ocean water. *Simulating Nature: Realistic and Interactive Techniques. SIGGRAPH*, 1:1–26, d. URL: https://people.computing.clemson.edu/~jtessen/reports/papers_files/coursenotes2004.pdf. 71, 72, 75, 78
- VARELA, J. AND GUEDES SOARES, C. Interactive simulation of ship motions in random seas based on real wave spectra. pages 235–244. URL: https://www.researchgate.net/publication/220868905_Interactive_Simulation_of_Ship_Motions_in_Random_Seas_based_on_Real_Wave_Spectra. 73
- YUKSEL, C. Real-time water waves with wave particles. URL: http://www.cemyuksel.com/research/waveparticles/cem_yuksel_dissertation.pdf. AAI3436772 ISBN-13: 9781124370330. 71, 73, 89
- YUKSEL, C., HOUSE, D. H., AND KEYSER, J. Wave particles. 26(3):99–es. ISSN 0730-0301. URL: <https://doi.org/10.1145/1276377.1276501>. 74

Appendices

A. Water velocity

The water height is deduced from system of equations described in Equations (1), and its solution according to Tessendorf is given by Equation (2) in Section 3. This appendix uses these equations to obtain an expression of the velocity potential and the water velocity. To simplify the derivation, only one wave vector \mathbf{k} is considered in Equation (2) as Equations (1) are all linear.

First, the velocity potential for $y = 0$ is deduced from first equation in 1, and Equations (2) and 3 as follows:

$$\begin{aligned}
 \phi(\mathbf{x}, 0, t) &= \int \frac{\partial \phi}{\partial t}(\mathbf{x}, 0, t) dt \\
 &= \int -gh(\mathbf{x}, t) dt \\
 &= -g \exp(i\mathbf{k} \cdot \mathbf{x}) \int \left(\tilde{h}_0(\mathbf{k}) \exp(i\omega(k)t) + \tilde{h}_0^*(-\mathbf{k}) \exp(-i\omega(k)t) \right) dt \\
 &= \frac{ig}{\omega(k)} \exp(i\mathbf{k} \cdot \mathbf{x}) \left(\tilde{h}_0(\mathbf{k}) \exp(i\omega(k)t) - \tilde{h}_0^*(-\mathbf{k}) \exp(-i\omega(k)t) \right) \quad (46)
 \end{aligned}$$

where $\mathbf{x} = \begin{bmatrix} x & z \end{bmatrix}^T$. It is assuming that potential velocity at any depth y can be written as follows:

$$\phi(\mathbf{x}, y, t) = \tilde{\phi}(\mathbf{k}, y, t) \exp(i\mathbf{k} \cdot \mathbf{x}). \quad (47)$$

Notice that this expression is convenient as it can be computed with an inverse Fast Fourier Transform. The function $\tilde{\phi}(\mathbf{k}, y, t)$ is defined as follows:

$$\tilde{\phi}(\mathbf{k}, y, t) = \frac{ig}{\omega(k)} E(\mathbf{k}, y) \left(\tilde{h}_0(\mathbf{k}) \exp(i\omega(k)t) - \tilde{h}_0^*(-\mathbf{k}) \exp(-i\omega(k)t) \right) \quad (48)$$

where *attenuation function* $E(\mathbf{k}, y)$ has to be determined from Equations 1. A first condition comes from Equation 46:

$$E(\mathbf{k}, 0) = 1 \quad (49)$$

Then, the second equation from system 1 can be imposed on the attenuation function. First, the left term is developed as follows:

$$\begin{aligned} \Delta\phi &= (-k_x^2 E(\mathbf{k}, y) - k_z^2 E(\mathbf{k}, y) + E''(\mathbf{k}, y)) \\ &\quad \times \frac{ig}{\omega(k)} \left(\tilde{h}_0(\mathbf{k}) \exp(i\omega(k)t) - \tilde{h}_0^*(-\mathbf{k}) \exp(-i\omega(k)t) \right) \exp(i\mathbf{k} \cdot \mathbf{x}) \\ &= (E''(\mathbf{k}, y) - k^2 E(\mathbf{k}, y)) \\ &\quad \times \frac{ig}{\omega(k)} \left(\tilde{h}_0(\mathbf{k}) \exp(i\omega(k)t) - \tilde{h}_0^*(-\mathbf{k}) \exp(-i\omega(k)t) \right) \exp(i\mathbf{k} \cdot \mathbf{x}) \end{aligned} \quad (50)$$

Hence, condition $\Delta\phi = 0$ is equivalent to find a solution of the following second order ordinary differential linear equation:

$$E''(\mathbf{k}, y) - k^2 E(\mathbf{k}, y) = 0. \quad (51)$$

It can be deduced that for $-H < y \leq 0$, $E(\mathbf{k}, y)$ is as follows:

$$E(\mathbf{k}, y) = C_1 \cosh(ky + C_2) \quad (52)$$

where $C_1, C_2 \in \mathbb{R}$ are constant. The derivative regarding height y of $\phi(\mathbf{x}, -H, t)$ can be rewritten as follows:

$$\begin{aligned} \frac{\partial\phi(\mathbf{x}, y, t)}{\partial y} &= \frac{\partial E(\mathbf{k}, y)}{\partial y} \frac{ig}{\omega(k)} \left(\tilde{h}_0(\mathbf{k}) \exp(i\omega(k)t) - \tilde{h}_0^*(-\mathbf{k}) \exp(-i\omega(k)t) \right) \exp(i\mathbf{k} \cdot \mathbf{x}) \\ &= kC_1 \sinh(ky + C_2) \\ &\quad \times \frac{ig}{\omega(k)} \left(\tilde{h}_0(\mathbf{k}) \exp(i\omega(k)t) - \tilde{h}_0^*(-\mathbf{k}) \exp(-i\omega(k)t) \right) \exp(i\mathbf{k} \cdot \mathbf{x}) \end{aligned}$$

Hence, at depth $y = -H$ the fourth equation of system 1 leads to:

$$\begin{aligned} \sinh(-kH + C_2) &= 0 \\ C_2 &= kH. \end{aligned} \quad (53)$$

The constant C_1 is obtained using Equation 49 as follows:

$$\begin{aligned} E(\mathbf{k}, 0) &= 1 \\ C_1 \cosh(C_2) &= 1 \\ C_1 &= \frac{1}{\cosh(kH)}. \end{aligned} \quad (54)$$

To resume, the full expression of the attenuation function for $-H \leq y \leq 0$ is as follows:

$$E(\mathbf{k}, y) = \frac{\cosh(ky + kH)}{\cosh(kH)}. \quad (55)$$

However, this expression cannot be used for large values of k and sea height H , where the hyperbolic cosine becomes bigger than the limit of real numbers even in double precision. Hence, E quickly reach the indeterminate form $\frac{\infty}{\infty}$. To fix this problem, the following physical assumption is made: it is assumed **deep water**, *i.e.* that the sea depth H tends towards ∞ . First, E is rewritten as follows:

$$\begin{aligned} E(\mathbf{k}, y) &= \frac{\cosh(ky + kH)}{\cosh(kH)} \\ &= \frac{\cosh(ky) \cosh(kH) + \sinh(ky) \sinh(kH)}{\cosh(kH)} \\ &= \cosh(ky) + \sinh(ky) \tanh(kH) \end{aligned}$$

Then, considering that $\lim_{H \rightarrow \infty} \tanh(kH) = 1$, the following approximation is obtained:

$$\begin{aligned} E(\mathbf{k}, y) &\approx \lim_{H \rightarrow \infty} E(\mathbf{k}, y) \\ &\approx \lim_{H \rightarrow \infty} \cosh(ky) + \sinh(ky) \tanh(kH) \\ &\approx \exp(ky). \end{aligned} \quad (56)$$

The third equation of the system 1 gives the following equality:

$$\frac{\partial h}{\partial t}(\mathbf{k}, t) = \frac{\partial \phi}{\partial y}(\mathbf{k}, 0, t) \quad (57)$$

Once again, we only considered one wave vector \mathbf{k} as Equations are all linear, in consequence Equation 57 becomes:

$$\begin{aligned} \frac{\partial \tilde{h}}{\partial t}(\mathbf{k}, t) - \frac{\partial \phi}{\partial y}(\mathbf{k}, 0, t) &= 0 \\ i\omega(k) \left(\tilde{h}_0(\mathbf{k}) \exp(i\omega(k)t) - \tilde{h}_0^*(-\mathbf{k}) \exp(-i\omega(k)t) \right) - \frac{igk}{\omega(k)} E(\mathbf{k}, 0) \\ &\times \left(\tilde{h}_0(\mathbf{k}) \exp(i\omega(k)t) - \tilde{h}_0^*(-\mathbf{k}) \exp(-i\omega(k)t) \right) = 0 \\ \omega(k) - \frac{gk}{\omega(k)} &= 0 \\ \omega(k) &= \sqrt{gk} \end{aligned} \quad (58)$$

This last Equation 58 gives the expression of the dispersion relation used in the Section 3.

Equation 56 and the definition of potential velocity $\nabla \phi = \mathbf{v}$ lead to the velocity \mathbf{v} . First, function $\tilde{\phi}$ is rewritten as follows:

$$\tilde{\phi}(\mathbf{k}, y, t) = \frac{ig}{\omega(k)} E(\mathbf{k}, y) \left(\tilde{h}_0(\mathbf{k}) \exp(i\omega(k)t) - \tilde{h}_0^*(-\mathbf{k}) \exp(-i\omega(k)t) \right). \quad (59)$$

Then the gradient of ϕ is as follows:

$$\nabla \phi = \begin{pmatrix} v_x \\ v_y \\ v_z \end{pmatrix} = \tilde{\mathbf{v}}(\mathbf{k}, y, t) \exp(i\mathbf{k} \cdot \mathbf{x}) \quad (60)$$

where $\tilde{\mathbf{v}}(\mathbf{k}, y, t)$ is the vector equal to:

$$\tilde{\mathbf{v}}(\mathbf{k}, y, t) = E(\mathbf{k}, y) \begin{pmatrix} \tilde{h}_0(\mathbf{k}) \exp(i\omega(k)t) - \tilde{h}_0^*(-\mathbf{k}) \exp(-i\omega(k)t) \\ \frac{-k_x g}{\omega(k)} \\ i\omega(k) \\ \frac{-k_z g}{\omega(k)} \end{pmatrix}, \quad (61)$$

Finally, reintroducing a sum on a set of waves vectors \mathbf{k} leads to:

$$\nabla \phi = \sum_{\mathbf{k}} \tilde{\mathbf{v}}(\mathbf{k}, y, t) \exp(i\mathbf{k} \cdot \mathbf{x}). \quad (62)$$

Note that the expression of $E(\mathbf{k}, y)$ (see Equation 56) is valid for height $y \leq 0$, but not usable above for $y > 0$. Several possibilities exist to overcome this problem:

1. The most naive one assumes $E(\mathbf{k}, y > 0) = 1$.
2. A more realistic solution is based on a linear extrapolation using the derivative at $y = 0$, as follows:

$$E(\mathbf{k}, y) = \begin{cases} E(\mathbf{k}, 0) + y \frac{\partial E}{\partial y}(\mathbf{k}, 0) & \text{if } y > 0, \\ \exp(ky) & \text{else.} \end{cases} \quad (63)$$

More sophisticated solutions are summarized in the Molin's book (2002) [Molin]. Nevertheless, they are too complex to compute as they make the attenuation function depending on $h(\mathbf{x}, t)$. For this reason, the Arc Blanc framework uses Equation 63, with the following simplified form:

$$E(\mathbf{k}, y) = \begin{cases} 1 + ky & \text{if } y > 0, \\ \exp(ky) & \text{else.} \end{cases} \quad (64)$$

B. Navier-Stokes equations approximation

This appendix proposes a derivation of Tessendorf's equations 1 from Navier-Stokes equations. As stated in Teman (2001) [Temam] and assuming conservation of mass, Navier-Stokes equations are given by:

$$\begin{cases} \frac{\partial}{\partial t}(\rho \mathbf{u}) + \mathbf{u} \cdot \nabla(\rho \mathbf{u}) = -\nabla p + \rho \mathbf{g} + \nabla^2(\rho \nu \mathbf{u}) \\ \frac{\partial}{\partial t}(\rho) + \nabla \cdot (\rho \mathbf{u}) = 0 \end{cases} \quad (65)$$

where $\mathbf{u} : \mathbb{R}^3 \mapsto \mathbb{R}^3$ is the flow velocity, ρ is the time-dependent density of the fluid, $p : \mathbb{R}^3 \mapsto \mathbb{R}$ is the pressure of the fluid, ν is the dynamic viscosity of the fluid. The first equation is called *Cauchy momentum equation* and the second *continuity equation*.

Boundary conditions are necessary for simulations. In the case of solid, the boundary equation is as follows:

$$\mathbf{u} \cdot \mathbf{n} = \mathbf{u}_{solid} \cdot \mathbf{n} \quad (66)$$

where, \mathbf{u}_{solid} is the velocity of the solid and \mathbf{n} is the normal to its surface.

Some assumptions are made to simplify these equations, and to derive Tessendorf equations. They are discussed below.

Incompressibility As mention in Section 3.3.2 of Hulin *et al.* (2001) [Hulin *et al.*], a fluid can be considered incompressible if $u \ll c_{sound}$ where c_{sound} is the sound speed in ocean which is approximately equal⁹. Aside from phenomena such as hurricane, this inequality seems reasonable for oceans, and leads to consider that ocean is incompressible. More formally:

$$\rho(t) = \rho. \quad (67)$$

Consequently, density can be factorized in each term of equations 65.

Inviscid A fluid can be considered inviscid if $Re \gg 1$ (see Section 2.3.1 of Hulin *et al.* (2001) [Hulin *et al.*]) where $Re = VL/\nu$ is the *Reynolds number* of the fluid defined by the order of magnitude of its velocity V , its characteristic length L and its dynamic viscosity ν . For Tessendorf derivation, V is the velocity of waves, L its wave length and for seawater at 20°C its is stated that $\nu = 1.0508 \cdot 10^{-6}$ (see the measure of the ITTC [ITTC]). Therefore, the inequality is true for product $VL \gg 10^{-5}$. For these values the ocean can be considered as flat. Hence, the viscosity term ν of Navier-Stokes equations 65 can be neglected.

Irrotational If a fluid is irrotational at time t_0 , it must remain irrotational unless there are changes in the boundary conditions. Clearly, flat sea are irrotational fluid, corresponding to $\nabla \times \mathbf{u} = \mathbf{0}$. Therefore, it can assume that for calm waves the fluid remains irrotational. Then, there exists a scalar field called **velocity potential** defined by $\phi = \nabla \phi$ from *Helmholtz decomposition*¹⁰.

These three assumptions lead to the Bernoulli equation (see Section 5.3.2 of Hulin *et al.* (2001), which is the following simplified version of the Cauchy momentum equation:

$$\frac{\partial \phi}{\partial t} + \frac{1}{2} \|\nabla \phi\|^2 + \frac{p}{\rho} + gy = 0 \quad (68)$$

Moreover, the continuity equation is now:

$$\Delta \phi = 0 \quad (69)$$

Nevertheless, these non-linear equations are still too complex to be solved at large scaled and in real-time.

Interface condition It is necessary to define a boundary condition at the interface between the ocean fluid and the air fluid. To simplify, it is assumed that the air can be represented as a region with constant pressure¹¹. Since air density is a hundred of times lighter than water, its effects on the free surface are assumed to be negligible. As with an incompressible fluid,

⁹See https://en.wikipedia.org/wiki/Sound_speed_profile to $c_{sound} = 1530 \text{ m.s}^{-1}$.

¹⁰See https://en.wikipedia.org/wiki/Helmholtz_decomposition.

¹¹As shown by the [barometric formula](#) the atmospheric pressure has a very low evolution in function of altitude.

only the differences in pressure matter. Therefore, the air pressure is defined as an arbitrary constant, leading to:

$$p = 0 \quad \text{at free surface.} \quad (70)$$

Hence, this allows to remove the pressure term in Bernoulli equation 68 at free surface.

Height field At this point, equations are still too complex to be used in real-time, especially in terms of dimension: it seems inconceivable to solve them at large scale in 3D. Therefore, to reduce their dimensions it is assumed that the surface geometry is described by a height field, as follows:

$$y = h(\mathbf{x}, t). \quad (71)$$

This hypothesis excludes a lot of physical phenomena like breaking waves, but it helps to reach large scale domain.

Free surface follows the velocity of water Next step assumes that the free surface follows the velocity of the water. Hence, for all \mathbf{x} on the horizontal axes at time $t + dt$ the height field is as follows:

$$h(\mathbf{x}', t + dt) = h(\mathbf{x}, t) + v_y dt \quad (72)$$

where:

$$\mathbf{x}' = \mathbf{x} + dt \begin{bmatrix} v_x \\ v_z \end{bmatrix} \quad (73)$$

The Taylor expansion of $h(\mathbf{x}', t + dt)$ leads to:

$$h(\mathbf{x}', t + dt) = h(\mathbf{x}, t + dt) + v_x dt \frac{\partial h(\mathbf{x}, t)}{\partial x} + v_z dt \frac{\partial h(\mathbf{x}, t)}{\partial z} + \dots \quad (74)$$

Neglecting the nonlinear terms in the Taylor expansion and reintegrating the development of $h(\mathbf{x}', t + dt)$ into Equation 72 and then dividing by dt leads to the following result:

$$\begin{aligned} \frac{h(\mathbf{x}, t + dt) - h(\mathbf{x}, t)}{dt} + v_x \frac{\partial h(\mathbf{x}, t)}{\partial x} + v_z \frac{\partial h(\mathbf{x}, t)}{\partial z} &= v_y \\ \frac{\partial h}{\partial t} + v_x \frac{\partial h}{\partial x} + v_z \frac{\partial h}{\partial z} &= v_y \end{aligned} \quad (75)$$

This leads to the following *advection equation*:

$$\frac{D}{Dt}(h(\mathbf{x}) - y) = 0 \quad (76)$$

Remove quadratic term The quadratic term in the Bernoulli equation 68 makes solving the equation too complex. Therefore, the velocity is assumed to be sufficiently small to neglect the quadratic term relative to the others. It leads to the “final” Bernoulli equation expressed as follows:

$$\frac{\partial \phi}{\partial t} = -gh(\mathbf{x}, t) \quad (77)$$

Smooth free surface Similarly, the nonlinear terms in the advection equation 76 make the equation’s resolution too complex. So the free surface height is assumed to be sufficiently smooth to neglect these terms relative to others. As a result, advection equation 76 becomes:

$$\frac{\partial h}{\partial t} = \frac{\partial \phi}{\partial y} \quad (78)$$

Flat ocean bottom Now, it is assumed that the ocean depth is constant, and equal to H . Then, the ocean floor is stationary and its normal to the ocean floor is $(0, 1, 0)$. Hence, boundary conditions at $y = -H$ are defined as:

$$\begin{aligned} \mathbf{u} \cdot \mathbf{n} &= 0 \\ \frac{\partial \phi}{\partial y} &= 0 \end{aligned} \quad (79)$$

Infinite ocean To avoid boundary conditions on \mathbf{x} , it is assumed that the ocean is horizontally infinite and periodic, allowing a finite simulation area. Therefore, the simulation area size is defined squared as $L \times L$. It leads to an ocean tile that can be infinitely duplicated.

Small free surface To simplify the location at which all equations are solved, it is assumed that the height of the free surface is sufficiently low. Hence, the equations can be solved at $\mathbf{x} = \mathbf{0}$.

Conclusion Finally, putting all together leads to the Tessendorf solution. More precisely, Tessendorf equations system is made from Equations (77), (69), (78), (79).

C. Two Fourier transforms in one

This section proposes a proof of Theorem 1.

Proof. This demonstration relies on the following formula that links the real part of the IFFT and the sum of the coefficients:

$$\mathcal{F}^{-1} \left(\frac{1}{2} (A + A^\dagger) \right) = \Re (\mathcal{F}^{-1} (A)) \quad (80)$$

where $A = (a_{n,m})$ is any Hermitian complex matrix of $M_n(\mathbb{C})$, and A^\dagger the transpose of its conjugate. Using the definition and linearity of the discrete Fourier transform, it follows for one term (k, l) of the IFFT:

$$\begin{aligned} \mathcal{F}^{-1} (A + A^\dagger)_{k,l} &= \mathcal{F}^{-1} (A)_{k,l} + \mathcal{F}^{-1} (A^\dagger)_{k,l} \\ &= \sum_{n,m} a_{n,m} \exp \left(-i \frac{2\pi}{N} (kn + lm) \right) + \sum_{m,n} a_{m,n}^* \exp \left(-i \frac{2\pi}{N} (km + ln) \right) \\ &= \sum_{n,m} (a_{n,m} + a_{n,m}^*) \exp \left(-i \frac{2\pi}{N} (kn + lm) \right) \\ &= 2\Re \left(\mathcal{F}^{-1} (A)_{k,l} \right) \end{aligned} \quad (81)$$

Since A is Hermitian by hypothesis, Equation (80) becomes:

$$\mathcal{F}^{-1} (A) = \Re (\mathcal{F}^{-1} (A)) \quad (82)$$

Applying this last equation to X and iY leads to:

$$\begin{aligned} \mathcal{F}^{-1} (X + iY) &= \mathcal{F}^{-1} (X) + i\mathcal{F}^{-1} (Y) \\ &= \Re (\mathcal{F}^{-1} (X)) + i\Re (\mathcal{F}^{-1} (Y)) \end{aligned} \quad (83)$$

□

D. Evaluation of the Number of Iterations for Convergence

The optimal number of iterations (N_{iter}) required for the iterative retrieval of water height was determined through two experiments, focusing on accuracy and computational efficiency.

The first experiment aimed to evaluate the number of iterations required for the water height computation to converge within a given precision. This test has been conducted on different wind speeds as it makes the height of water significantly. Wind speeds ranged from 0.1 m/s to 35 m/s in 0.5 m/s increments, with convergence tested at 10^3 random positions uniformly distributed over a $10^4 \times 10^4$ m domain. The iterative process was repeated until the difference between consecutive height estimates was smaller than 0.01 m. The results, shown in Figure 17, indicate that the required number of iterations increases with wind speed but stabilizes at approximately $N_{\text{iter}} = 4$ for higher wind speeds.

The second experiment aimed to measure the computational cost associated with varying numbers of iterations. The execution time was assessed using a CUDA-based implementation, where the iterative retrieval of water height was performed for different values of N_{iter} . Each test was executed 10^3 times on a GPU, and execution times were recorded across 10^5 randomly sampled positions. The measurements included the minimum, maximum, mean, and variance of execution times for each iteration count. The results, presented in Figure 18, show that while execution time increases with the number of iterations, the rate of increase diminishes after four iterations. This confirms that $N_{\text{iter}} = 4$ provides an optimal balance between computational efficiency and accuracy, ensuring reliable convergence across tested conditions.

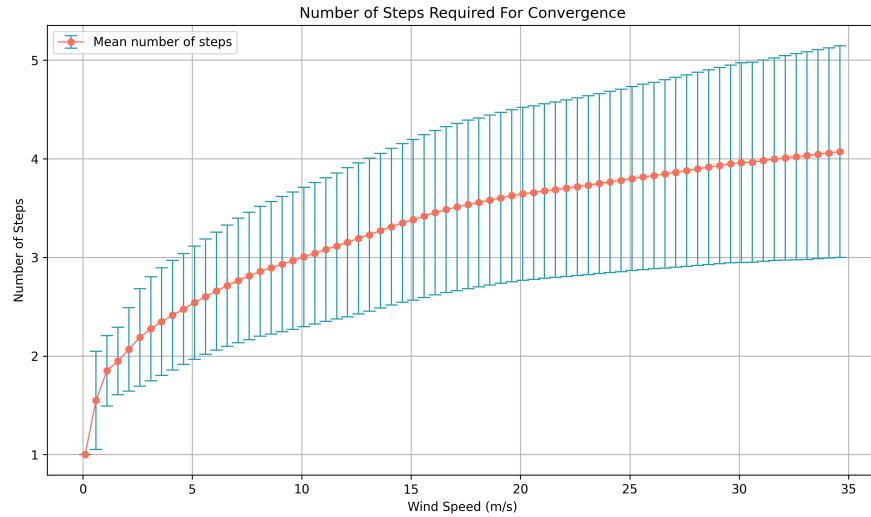


Figure 17. Mean number of steps required for convergence as a function of wind speed. Error bars represent the variance of iterations across 1000 test points.

Index of Supplemental Materials

Three supplemental videos are included:

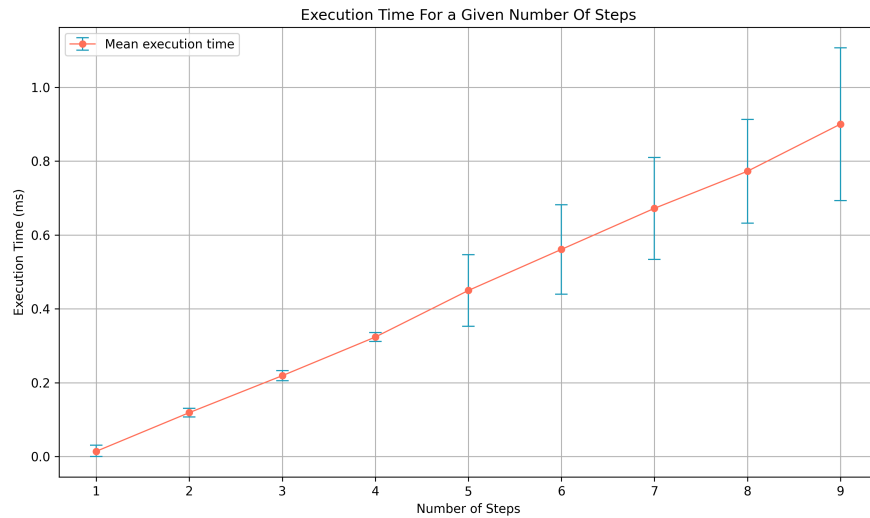


Figure 18. Average execution time per iteration count over 1000 tests, measured across 10^5 sample positions. Error bars indicate variance in execution time.

- <https://jcgt.org/published/0014/01/05/timelapse.mp4>
Time lapse video.
- <https://jcgt.org/published/0014/01/05/lateralMovingBoat.mp4>
Video of a boat moving across the field of view.
- <https://jcgt.org/published/0014/01/05/fixedOutsideMotorBoatMoving.mp4>
Wider view, including sun and boat moving away from the camera.

Author Contact Information

David Algis
Bât. H1 - SP2MI
TSA 41123
86073 Poitiers Cedex 9
FRANCE
david.algis@univ-poitiers.fr

Bérenger Bramas
INRIA Nancy
berenger.bramas@inria.fr

Emmanuelle Darles
Université de Poitiers
emmanuelle.darles@univ-poitiers.fr

Lilian Aveneau
Université de Poitiers
lilian.aveneau@univ-poitiers.fr

David Algis, Bérenger Bramas, Emmanuelle Darles, Lilian Aveneau, Arc Blanc: a real time ocean simulation framework, *Journal of Computer Graphics Techniques (JCGT)*, vol. 14, no. 1, 70–115, 2025
<http://jcgt.org/published/0014/01/05/>

Received:	2024-01-31		
Recommended:	2025-01-09	Corresponding Editor:	Angelo Pesce
Published:	2025-03-05	Editor-in-Chief:	Eric Haines

© 2025 David Algis, Bérenger Bramas, Emmanuelle Darles, Lilian Aveneau (the Authors).
The Authors provide this document (the Work) under the Creative Commons CC BY-ND 3.0 license available online at <http://creativecommons.org/licenses/by-nd/3.0/>. The Authors further grant permission for reuse of images and text from the first page of the Work, provided that the reuse is for the purpose of promoting and/or summarizing the Work in scholarly venues and that any reuse is accompanied by a scientific citation to the Work.

